Journal of Energy Storage 101 (2024) 113948

Contents lists available at ScienceDirect

Journal of Energy Storage

journal homepage: www.elsevier.com/locate/est

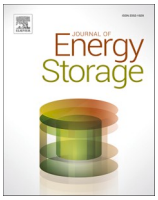

Research papers

Assessing the influence of compressor inertia on the dynamic performance of large-scale vapor compression heat pumps for Carnot batteries

Robin Tassenoy [a,*], Antoine Laterre [b,c], Vincent Lemort [c], Francesco Contino [b], Michel De Paepe [a,d,e], Steven Lecompte [a,d]

[a] Department of Electromechanical, Systems and Metal Engineering, Ghent University, Sint-Pietersnieuwstraat 41, Ghent 9000, Belgium
[b] Institute of Mechanics, Materials and Civil Engineering (iMMC), Université catholique de Louvain (UCLouvain), Place du Levant 2, Louvain-la-Neuve 1348, Belgium
[c] Thermodynamics Laboratory, University of Liège (ULiège), Allée de la Découverte 17, Liège 4000, Belgium
[d] FlandersMake@UGent – Core lab MIRO, Ghent 9000, Belgium
[e] Department of Mechanical Engineering, University of Cape Town, Private Bag X3, Rondebosch 7701, South Africa

ARTICLE INFO

Keywords:
Carnot batteries
Pumped thermal Energy storage
Heat pump
Grid balancing
Frequency regulation
Dynamic model

ABSTRACT

Carnot batteries, a combination of a power-to-heat, a thermal storage and a heat-to-power system, are an emerging storage technology that could provide a solution to the imbalance of intermittent renewable energy injection into the grid. However, which grid services this technology could deliver remains unclear due to a lack of detailed research on the system dynamics, which makes it difficult to predict, control and optimize its performance in actual operating conditions. As such, also the financial appraisal of the technology remains unclear. This work explores the potential of delivering grid balancing services during the charging phase of a Rankine-based Carnot battery. In this context, the electrical response of the vapor compression heat pump is of interest rather than the thermal response, as it is crucial for integration of the storage system in the electrical grid. Therefore, the dynamic behavior of a 1.5 MWe vapor compression heat pump is addressed. A control strategy driven by the requirements of the electrical grid was implemented and the effect of compressor rotational inertia was taken up into the modelling approach. The prequalification tests for grid balancing services in the central European grid were simulated using models neglecting and considering rotational inertia. While the rotational inertia can be considered negligible for thermodynamic performance predictions, which remain dominated by the thermal capacitances and refrigerant reservoirs in the closed loop, this work shows it is relevant to variable-speed heat pump applications for correct simulation of the electrical response. The heat pump can deliver a capacity of 750 kW for secondary and tertiary reserve in the upward and downward direction, both neglecting and considering rotational inertia. However, its potential to deliver a symmetric primary reserve capacity of 375 kW is identified only when the rotational inertia is included in the modelling. Grid balancing services during the charging phase can thus be additional revenue streams to increase the financial feasibility of Carnot batteries and it is therefore worthwhile to investigate their potential financial benefits.

1. Introduction

The share of renewables in the European power mix is continuously increasing, peaking at 43 % in 2022 [1]. This large deployment of variable renewable energies (VRE) challenges the stability of the electrical grid due to their intermittent nature. Energy storage can address these problems by power and voltage smoothing, energy management, frequency control, peak shaving, load leveling, seasonal storage and standby generation during a fault [2]. Therefore, energy storage is considered one of the main drivers to provide the flexibility required to decarbonize the electricity grid [3,4].

Carnot batteries are an emerging large-scale electrical energy storage (EES) concept that may provide additional flexibility to the grid. The concept involves three steps. First, electrical energy is converted into heat using a heat pump or Joule heater after which the heat is stored in the second step. Finally, heat engine technology is used to convert the heat back to electricity when needed. One of the Carnot battery's subsets is pumped thermal energy storage (PTES), in which an electrically driven heat pump elevates the temperature of heat coming from a cold source and delivers this to a thermal storage system at higher temperature [5]. So far, mainly the steady-state analysis and optimization of the

* Corresponding author.
E-mail address: Robin.Tassenoy@UGent.be (R. Tassenoy).

https://doi.org/10.1016/j.est.2024.113948
Received 17 May 2024; Received in revised form 18 September 2024; Accepted 21 September 2024
Available online 1 October 2024

Nomenclature

Greek and Latin symbols

Δ	difference
η	efficiency
ρ	density [kg/m^3]
τ	torque [N·m]

Sub- and superscripts

0	instant of step in controller setpoint
comp	compressor
cond	condenser
drive	drive side
el	electrical
HX	heat exchanger
I	integrator
in	inlet
is	isentropic
nom	nominal
out	outlet
r	refrigerant
set	setpoint
vol	volumetric

Symbols

a	fitting constant
abs	absolute
aFRR	automatically activated frequency restoration reserve, secondary reserve
BSP	balance service provider
EES	electrical energy storage
FAT	full activation time
FCR	frequency containment reserve, primary reserve
FV	finite volume
h	enthalpy [J/kg]
I	rotational inertia [kg·m^2]
k	proportional constant
$\dot{m}$	mass flow rate [kg/s]
mFRR	manually activated frequency restoration reserve, tertiary reserve
MARI	Manually Activated Reserves Initiative
n	rotational speed [Hz]
p	pressure
P	power
PHE	plate heat exchanger
PICASSO	Platform for the International Coordination of Automated Frequency Restoration and Stable System Operation
PP	pinch point [°C / K]
PR	pressure ratio
PTES	pumped thermal energy storage
$\dot{Q}$	heat transfer rate [W]
qh	quarter hour
RMSE	root-mean-squared-error
s	entropy [J/(kgK)]
SA	scheduled activation
SH	superheat [°C / K]
t	time [s]
T	temperature [°C / K] / integral time
TES	thermal energy storage system
TSO	transmission system operator
VRE	variable renewable energies
WF	working fluid
x	time-varying variable

storage concept and the obtainable round-trip efficiencies were studied [6]. More recently, the techno-economic performance and optimization of PTES have gained interest as well. Vecchi et al. [7] collected and compared the techno-economic performance data of different Carnot battery systems in the literature. Moreover, they discussed the applications of Carnot batteries at energy system scale and the most recent commercial developments in Carnot battery technologies. The literature reveals that Carnot batteries have been considered mainly for load-shifting and arbitraging services. The revenues they can generate by these services are limited due to their relatively low round-trip efficiency, both in design and off-design conditions. Consequently, the initial investment cost can typically not be recovered and Carnot batteries are mostly not financially viable considering load-shifting and arbitraging services alone. Similar observations were made for utility scale battery systems where it was shown that service stacking is required to reach a profitable business model, even despite their higher round-trip efficiency compared to Carnot batteries [8,9]. Based on the literature, PTES thus needs further efficiency improvements, cost reductions and a portfolio of grid services to provide additional revenue streams.

1.1. Grid balancing services

Grid flexibility is usually defined as the possibility of modifying generation and/or use patterns in reaction to an external signal (e.g. price) to contribute to the power system stability in a cost-effective manner. At the transmission grid level, flexibility is linked to grid balancing services offered to transmission system operators (TSOs) [10]. These grid balancing services are considered one of the most contributing cash flows during service stacking with energy storage systems [8,11]. They offset potential mismatches between the instantaneous electricity production and demand, which is essential to ensure stable grid operation. Three balancing products can be distinguished based on their time scale: primary or frequency containment reserve (FCR), secondary or automatically activated frequency restoration reserve (aFRR) and tertiary or manually activated frequency restoration reserve (mFRR). The delivery of FCR is always symmetric, meaning the power should be controllable in a power band around the nominal operating point. aFRR and mFRR can be delivered either up- or downward, or in both directions. A summary of the main service characteristics is presented in Table 1.

Table 1
Characteristics of balancing services in the central European electricity grid.

Balancing service	Direction	Full activation time	Min. delivery time	Min. bid size	Ref.
FCR	symmetric	30 s	15 min	1 MW	[12,13]
aFRR	up / down	7.5 min (to 5 min)	15 min	1 MW	[14,15]
mFRR	up / down	15 min (to 12.5 min)	5 min	1 MW	[16]

1.2. Dynamic modelling of PTES and utility scale heat pumps with respect to grid balancing services

The discussion above clearly illustrates the importance of the power dynamics of electrical storage systems for the delivery of grid balancing services. However, detailed research on these dynamics is lacking for PTES, which makes it difficult to predict, control and optimize their performance in actual operating conditions [17]. Laterre et al. [18] explicitly highlighted the need for characterization of the dynamic performance before considering the added value of grid services in their techno-economic analysis of PTES.

This knowledge gap has partially been addressed for Brayton-based PTES recently [17,19,20]. Studies on the system start-up behavior [17], step response to control parameters [19] and transient behavior of the storage system during cyclic charging- and discharging were published [20]. The design of a suitable control system to maintain a desired power uptake as needed for delivery of grid balancing services was not discussed so far.

Similar observations can be made for the Rankine-based PTES systems. The operation of such systems under variable operating conditions has been studied by quasi-steady state modelling in different scenarios [21,22]. While this quasi-steady modelling approach is useful to perform yearly simulations with a 1 h-timestep, this approach does not allow for a detailed assessment of the transients at time scales relevant for grid balancing services. The shorter-term dynamics of the thermal storage system of a CHEST system integrated with a cascaded PCM storage were recently studied during the charging- and discharging process [23]. The power response of the charging- or discharging cycle relevant for grid balancing services was not discussed however as these cycles were optimized in quasi-steady state.

The detailed dynamics and control of a full Rankine-based PTES-system or its vapor compression charging cycle for delivery of grid balancing services are not available in the literature, to the best of the authors' knowledge. Focusing on the charging cycle, large-scale stand-alone heat pumps are mainly applied in district heating applications, where they are not optimized to respond quickly to the needs of the electrical grid. Nevertheless, some research has been performed on this topic. Meesenburg et al. [24] developed a numerical model of a two-stage ammonia heat pump with piston compressors used in district heating and calibrated this model on experimental data. They showed that the electrical power uptake could be controlled from 250 kWe to 175 kWe in 54 s and from 250 kWe to 100 kWe in 99 s without the risk of condensation in the suction line, after optimization of the control strategy. At larger scale, Wolscht et al. [25] recently presented an experimentally validated dynamic model of a 10.5 MWe heat pump based on the transcritical CO_2 cycle and radial turbocompressor technology. They analyzed the open-loop dynamic behavior of the system. The results showed fast power dynamics where the compressor power was varied by 80 % compared to the maximum power within 45 s by reducing the compressor speed by 60 % within 30 s and simultaneously opening the expansion and expander bypass valves. The authors thus demonstrated fast power dynamics in response to set changes to the actuators. However, no control system to steer these actuators to obtain a desired power uptake was developed so far. Consequently, providing grid flexibility using large-scale vapor compression heat pumps is not well understood [26].

1.3. Scope of this study

Electrical energy storage systems require a fast electric power response to deliver grid balancing services. So far, the dynamic response and control of PTES driven by the requirements of the electrical grid remains a clear gap in the literature. No study discussing the dynamic power response of a complete Rankine-based PTES or its charging cycle has been found. Only a few studies address this topic for stand-alone grid-scale heat pumps. However, these all focus on heat pumps for district heating applications which were not optimized for a fast electrical response. It thus remains unclear if the vapor compression heat pump can deliver grid balancing services during the charging phase of the PTES. Moreover, all studies mentioned model the compressor in steady-state. The compressor rotational inertia is thus disregarded. This is a common approach in the modelling of thermal systems due to the slow thermal responses of the heat exchangers compared to the rotating machinery [24,27–29]. While the rotating inertia can be considered negligible for thermodynamic performance predictions, which remain dominated by thermal capacitances and refrigerant reservoirs in the closed loop, it raises the question whether this rotational inertia may be significant when focusing on the electrical power response of variable-speed heat pumps in the context of grid balancing services. These observations translate to three crucial research goals:

- To analyze the dynamic behavior and control with respect to fast electrical power control of large-scale variable-speed vapor compression heat pumps. This includes following the optimal set-point of power response, heat flows and delivery temperatures.
- To quantify the impact of the rotational inertia on the electrical response, as this is often disregarded when the thermal response is of interest but may be significant with respect to the electrical response.
- To determine which grid balancing services heat pumps could deliver to explore additional revenue streams for PTES during the charging phase.

This work is carried out in the context of Carnot batteries, where the electrical power response of the charging system is crucial for integration of the EES within the electrical grid. This is in contrast to traditional heating applications of heat pumps, where the thermal response is of interest. Although the boundary conditions of the heat pump are selected based on a Carnot battery case study, the results obtained are generally applicable to large-scale variable-speed heat pump applications where correct simulation of the power response is of interest.

As the rotational compressor inertia was taken up in the modelling approach, this work thus provides novel insights in the dynamical modelling of variable-speed vapor compression heat pumps with respect to their electrical power response and the design of corresponding control strategies. Moreover, demonstration of the heat pump's capacity to deliver these grid balancing services opens up new grid-related applications and integration scenarios for large-scale heat pumps and PTES. It also allows to consider these services as additional revenue streams in techno-economic assessments of PTES – which may significantly affect the financial feasibility of the storage technology and thus its further uptake within the energy system.

In this work, a dynamic model of a 1.5 MWe vapor compression heat pump cycle using a twin-screw compressor was constructed (Sections 3.1 and 3.2). Then, a suitable control strategy was developed to follow the desired power uptake, while maintaining correct delivery temperatures (Section 3.3). Finally, the model verification against available information in the literature was discussed (Section 3.4). The verified model was used to analyze the system dynamics and control by studying the system's step response, focusing on the influence of rotational inertia (Section 4.2). Finally, the controlled system was validated against prequalification tests for grid balancing services in the central European grid issued by the Belgian TSO. As such, its technical potential to deliver tertiary reserve (Section 4.3.1), secondary reserve (Section 4.3.2) and primary reserve (Section 4.3.3) was assessed.

2. Case study and topology selection

As explained before, this work discusses the dynamic modelling of vapor compression heat pumps in the context of Carnot batteries. In such a PTES, the vapor compression heat pump converts electrical energy from the grid to heat, which is stored in the thermal storage system, as shown schematically in Fig. 1.

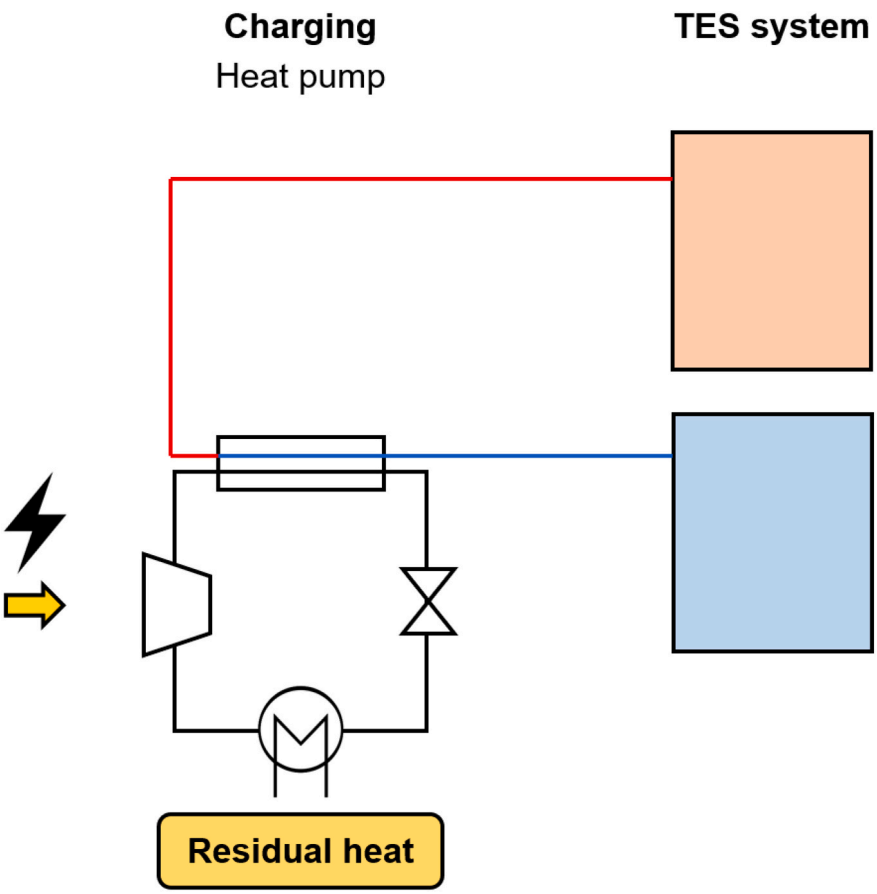

Fig. 1. Schematic representation of a vapor compression heat pump in a thermally integrated PTES.

While several applications have been proposed, Rankine-based PTES typically takes advantage of a low-grade heat source to boost the electric round-trip efficiency of the system [30]. Apart from low grade geothermal heat and solar thermal energy, heat sources of suitable thermal capacity and temperature level can be found in industry. According to Marina et al. [31] promising residual heat sources are available mostly in the refinery, chemical, paper and food sector. In this work, residual heat available in the pulp and paper industry is considered as heat source. However, significant amounts of residual heat at similar temperature and power levels are available in other sectors [31], making the results more generally applicable.

In this specific study, residual heat at a temperature of 60 °C coming from the waste water of a paper pulp plant is assumed based on personal communication with a paper manufacturer. A volume flow rate of 200 m^3/h of waste water is currently cooled to 40 °C by a cooling tower, resulting in an available thermal heat source of 4.57 MWth.

Within this temperature range, sensible liquid heat storage is often applied in Rankine-based PTES as it is reliable, mature and cost-efficient. A two-tank configuration guarantees almost constant charge and discharge profiles. It was thus selected instead of a single tank solution, despite the cost of doubling the storage volume [30,32]. Water tanks were opted for as they are cheap, have low environmental impact, are suitable for the temperature range of interest and are commercially available for large capacities [6,33]. The hot tank temperature was chosen at 95 °C, while a cold tank temperature of 70 °C was assumed. This specific hot temperature was chosen to avoid pressurizing the tanks, which reduces the investment and maintenance costs [34]. The cold tank temperature of 70 °C was considered based on the trade-off between efficiency and storage density [18,32,35]. These temperatures are within the operational limits of commercial heat pumps currently available [36,37].

The basic topology considered consists of the four main heat pump components: an evaporator, a compressor, a condenser and an expansion valve. In the literature, several advanced heat pump cycles have been proposed, including internal recuperation with a recuperator [32,36,38]. Although advanced cycles result in high coefficients of performance, the additional components increase the thermal capacitance of the system and are thus expected to slow down the system's dynamic response. Moreover, complex cycles require careful, simultaneous coordination of different control loops, which may further limit the obtainable ramping rates [38]. Therefore, a basic system was assessed first. More complex topologies can be addressed in follow-up studies if this basic system proves to be suitable to deliver grid balancing services.

3. Simulation approach

Once the boundary conditions and general topology were determined, the nominal cycle conditions were calculated in more detail. Based on these nominal conditions, suitable components were selected and modelled. These components were combined in a full dynamic model after which the control system was designed. Then, the model was verified based on available information in the literature. Finally, a brief discussion on the test criteria was provided.

3.1. Refrigerant selection and nominal operation conditions

The case study and its boundary conditions above impose the temperature range of the heat pump. Based on several studies, R-1233zd(E) was selected because it shows good thermodynamic performance in the intended operating range and has a low global warming and ozone depletion potential compared to refrigerants commonly used

Table 2
Nominal operating conditions: modelling assumptions.

Assumed parameter	Value	Unit
$T_{water,source,in}$	60	°C
$T_{water,source,out}$	40	°C
$\dot{m}_{source}$	54.6	kg/s
$T_{hot\ tank}$	95	°C
$T_{cold\ tank}$	70	°C
p_{tanks}	1	bar
$PP_{evaporator}$	5	°C
$PP_{condenser}$	5	°C
Δp_{HX}	0	Pa
$SH_{compressor,in}$	3	°C
$SC_{valve,in}$	Maximized	°C
$\eta_{is,compressor}$	0.75	–
Refrigerant	R-1233zd(E)	–
TES fluid (hot and cold tank)	Water	–

[37,39,40]. Once the refrigerant was selected, the nominal operating conditions of the heat pump were determined using the steady-state cycle model described by Laterre et al. [35]. Fluid property data were imported from REFPROP 10.0 [41]. Table 2 provides an overview of the boundary conditions and assumptions applied. For the intended power, both radial and twin-screw compressors would be feasible. Here, a variable-speed twin-screw compressor was opted for thanks to its high part-load efficiency and wide operating range [42]. Moreover, they are applied in commercially available heat pumps in the intended capacity range [37]. A compressor isentropic efficiency of 75 % was assumed to determine the nominal conditions [43,44].

The resulting nominal operating conditions are summarized in Table 3. The Ts- and ph-diagram of the cycle are shown in Fig. 2 (a) and (b), respectively. In the Ts-diagram, it is clear that the subcooling is maximized depending on the pressure levels and heat exchanger pinch points. This choice can be understood from the ph-diagram. Maximizing the subcooling increases the cooling effect in the condenser (extending the diagram to the left), while keeping the compression work equal (as the pressure levels do not change). This increases the COP. The value of 24.4 °C thus results from the assumed basic topology, the given condenser pinch point and the relatively high temperature glide in the condenser. This basic steady-state model is used to calculate relevant nominal conditions allowing component selection, rather than cycle optimization.

3.2. Component selection and modelling

The dynamic heat pump model was programmed in the object-oriented modelling language Modelica [45], using Dymola 2022 [46] and the TIL-library 3.14.0 [47]. The component models of the TIL-library were extended when necessary, the details are found further in this work. Fluid properties were calculated using the REFPROP-database [41].

Table 3
Nominal operating conditions: results.

Output parameter	Value	Unit
$p_{evaporator}$	1.83	bar
$p_{condenser}$	10.29	bar
Pressure ratio	5.61	–
$T_{evaporation}$	99.4	°C
$T_{condensation}$	35.0	°C
$\dot{m}_{WF}$	33.25	kg/s
$\dot{m}_{tank\ storage}$	57.05	kg/s
$\dot{Q}_{evaporator}$	4.57	MW
$\dot{Q}_{condenser}$	5.99	MW
$P_{compressor}$	1.42	MW
COP	4.2	–

3.2.1. Heat exchangers

Plate heat exchangers (PHEs) were selected for both the evaporator and condenser because they are relatively cheap, compact and have a modular design [28,32]. Gasketed PHEs with capacities up to 30 MWth and volume flow rates up to 4500 m^3/h are available [48].

The minimum cross-sectional flow area and surface area in a PHE are interdependent, making precise matching of the thermal and hydrodynamic load difficult [49]. In the current application, rather high volume flow rates were required, especially in the evaporator, making the heat exchanger pressure drop the dominant sizing constraint. Therefore, smaller plates and more parallel flow channels were selected to increase the cross-sectional area and thus reduce the pressure drop. Funke FP205 plates were selected [48]. For the evaporator, two FP205 heat exchangers with 500 plates were used in parallel. For the condenser, one FP205 heat exchanger with 500 plates was used.

The 1D finite volume (FV) model from the TIL-library [47] was used to model the PHEs, assuming countercurrent flow. FV-models have proven reliable for the dynamic simulation of evaporators and condensers [28]. Moreover, this PHE-model of the TIL-library was successfully used to simulate the dynamic behavior of large-scale heat pumps [24,50,51]. The plate dimensions of the Funke heat exchangers were used as model input. As the internal geometry is not published by the manufacturer, a reasonable assumption was made based on the literature. Typical corrugation depths of (industrial) heat exchangers range from 1.5 to 5.4 mm, resulting in identical plate spacing [49,52]. In this work, an inside geometry based on the one tested by Lee et al. [53] was used. Although this geometry was used to study evaporation, similar geometries were used to study condensation [54,55]. The heat exchanger studied by Lee et al. [53] has a corrugation depth of 1.94 mm, a pitch length of 7.5 mm and a chevron angle of 60°. Given the higher capacities required in this study, the corrugation depth and pitch length were doubled to deal with the higher volume flow rates, while the chevron angle of 60° was maintained. These updated dimensions still fall within the common range. The heat transfer correlations used are listed in Table 4.

Lee et al. [53] proposed a correlation for evaporation temperatures between 60 and 80 °C and refrigerant mass fluxes between 32 and 58 $\frac{kg}{m^2 s}$. The temperature range is thus higher than in this work, but the evaporation temperature was shown to have almost no effect on the heat transfer. The mass flux in nominal conditions is 32.54 $\frac{kg}{m^2 s}$. The flux was chosen at the low end to limit flow velocities and thus pressure drop. The correlation by Zhang et al. [55] was fitted based on condensation temperatures up to 90 °C, which is just below the range in this study. The correlation has been validated outside the fitting range with satisfactory results and is sufficient to capture the main trends. As a validity check, both heat transfer correlations were compared to the correlations of Longo et al. [58,59], which were already available in the TIL-library. For both, the deviation was below 18 % which was within the uncertainty range on the correlations. Therefore, the selected two-phase correlations were found to be acceptable and correctly implemented.

The pressure drop correlations proposed by Lee et al. [53] and Zhang et al. [55] were implemented for evaporation and condensation, respectively. The correlation of Martin [57] was used for the single phase region and water side. The plate dimensions and number of plates were deliberately chosen to provide a sufficiently high cross-sectional flow area. At nominal operating conditions, pressure drops of 0.30 and 0.22 bar were calculated for the evaporator and condenser respectively.

3.2.2. Compressor

The nominal operating conditions of the compressor were determined based on the steady-state cycle calculation discussed in Section 3.1. Taking the required volume flow rates and pressure ratio into account, a rotary screw or centrifugal compressor would be the most suitable option [37,60]. A variable-speed twin-screw compressor was

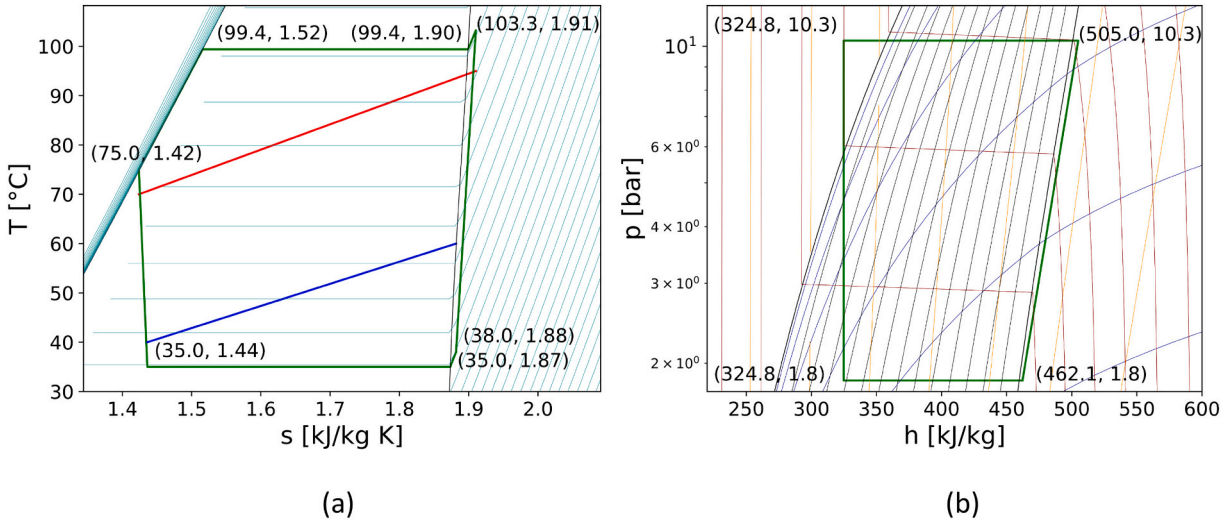

Fig. 2. Heat pump cycle in nominal operating conditions (a) Ts-diagram (b) ph – diagram. The source (blue line) and sink (red line) in the Ts-diagram are indicative only but give a good representation of the cycle. (For interpretation of the references to colour in this figure legend, the reader is referred to the web version of this article.)

Table 4
Heat transfer correlations.

Type	Correlation	Reference
Evaporation	Lee et al., 2018	[53]
Condensation	Zhang et al., 2021	[55]
Single phase	Chisholm and Wanniarachchi	[56]
Water side	Martin, 2010	[57]

selected as it maintains a high part-load efficiency in a wide range of part-load conditions [42]. Moreover, a recent market study illustrates that volumetric machines are often opted for in high temperature heat pumps with comparable capacity [37].

Volumetric compressors can be modelled effectively using a semi-empirical approach according to the method proposed by Lemort [61]. This method was successfully applied to screw machines. However, publications including the calibrated parameter values focus on small capacity machines [62,63]. As these models are only extrapolatable in a small range [64], these values cannot be used in the current study. The approach was successfully applied to a MW-compressor recently [51], but the machine characteristics were normalized and the calibration values were not published.

As no suitable calibration data was available, an alternative performance-map-based approach was followed in this work. This strategy was proven successful in similar studies analyzing large-scale heat pumps using turbomachinery [27,65]. To characterize the volumetric twin-screw compressor, the isentropic and volumetric efficiency should be known as a function of the operational parameters. Therefore, performance data from a suitable twin-screw compressor with variable internal volume ratio was retrieved from the RTSelect-software of GEA Heating & Refrigeration technologies [66]. The main compressor characteristics, as indicated by the manufacturer, are summarized in Table 5. An overview of the operating characteristic is shown in Fig. 3.

Table 5
Twin-screw compressor characteristics as indicated by the manufacturer [66].

Characteristic	Value	Unit
V_s	0.065	m^3
Internal volume ratio range	2.2–3.8	–
Speed (min)	25	Hz
Speed (max)	60	Hz
Rotational inertia	15,497	$kg{\cdot}m^2$

Based on this raw data, polynomials for the isentropic and volumetric efficiency were constructed in Python 3.7 [67]. A second-degree polynomial was proposed for both efficiencies:

$$\begin{aligned}\eta = {} & a_0 + a_1\left(\frac{n}{n_{nom}}\right) + a_2\left(\frac{\rho_{comp,in}}{\rho_{comp,in,nom}}\right) + a_3\left(\frac{PR}{PR_{nom}}\right) + a_4\left(\frac{n}{n_{nom}}\right)^2 \\ & + a_5\left(\frac{\rho_{comp,in}}{\rho_{comp,in,nom}}\right)^2 + a_6\left(\frac{PR}{PR_{nom}}\right)^2 + a_7\left(\frac{n}{n_{nom}}\right)\left(\frac{\rho_{comp,in}}{\rho_{comp,in,nom}}\right) \\ & + a_8\left(\frac{n}{n_{nom}}\right)\left(\frac{PR}{PR_{nom}}\right) + a_9\left(\frac{\rho_{comp,in}}{\rho_{comp,in,nom}}\right)\left(\frac{PR}{PR_{nom}}\right)\end{aligned} \quad (1)$$

with a_i the fitting coefficients, n the compressor rotational speed in Hz, $\rho_{comp,in}$ the density at the compressor inlet [kg/m^3] and PR the pressure ratio over the compressor. These latter quantities were normalized by their nominal values to ensure equal weighting of the different coefficients during the fitting process. The respective nominal conditions were $n_{nom} = 60\ Hz$, $\rho_{comp,in,nom} = 9.867\ kg/m3$ and $PR_{nom} = 5.618$. The fitting coefficients were determined by minimizing the least-squares error between the performance map and the polynomial prediction. The resulting coefficients are shown in Table 6. The resulting polynomials predict the compressor performance well, as indicated by the mean and maximum absolute deviations shown in Table 7. As these polynomials are fitting results, it is important to provide performance data spread over the whole use range and be cautious with extrapolation. Nevertheless, the proposed polynomials are a numerically efficient and stable way of capturing the compressor trends.

The polynomials discussed above were used to extend the *EffCompressor*-model of the TIL-library [47]. The performance maps take the part-load performance of the compressor into account, but neglect the thermal capacitance and rotational inertia of the component. The rotational inertia was added to the TIL-model. Two versions of the compressor model were considered: without and with rotational inertia. First, the rotational inertia of the component was neglected, as commonly done in dynamic modelling of thermal cycles [24,28,29]. In the model with inertia, the rotational inertia of the selected compressor according to the manufacturer data [66], $I = 15\,497 kg{\cdot}m^2$, was taken into account to assess whether it is relevant with respect to the system's electrical power response. The thermal capacitance of the compressor was neglected as the heat pump is operating before the delivery of grid balancing services and was thus assumed to be warm. As this thermal capacitance is small compared to the thermal capacitance of the heat exchangers, it was assumed negligible during the power ramping for

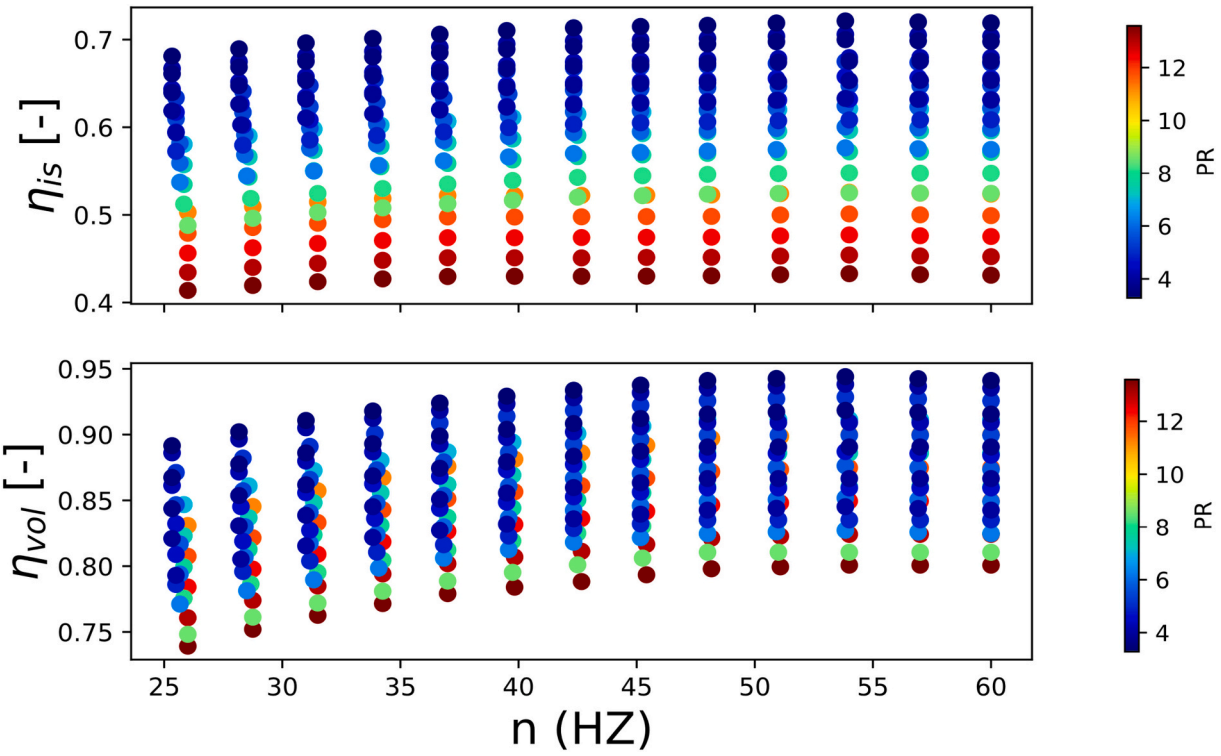

Fig. 3. Isentropic and volumetric efficiency characteristics of a twin-screw compressor.

Table 6
Fitting coefficients efficiency polynomials twin-screw compressor (rounded to 3 significant digits).

Coefficient	η_{is}	η_{vol}
a_0	1.03	1.09
a_1	0.371	0.488
a_2	−0.0383	0.135
a_3	−0.243	0.00455
a_4	−0.150	−0.245
a_5	0.00799	−0.0323
a_6	0.0455	0.00609
a_7	−0.0444	−0.0394
a_8	−0.0472	−0.00377
a_9	−0.307	−0.533

Table 7
Absolute root mean square error and maximum error for efficiency polynomials twin-screw compressor.

Fit	RMSE [% abs]	Max error [% abs]
η_{is}	0.228	0.752
η_{vol}	0.156	0.532

grid balancing services. The influence of the compressor thermal capacitance on the system's start-up behavior (where the compressor is cold before) will be assessed in future work.

3.2.3. Valve

The *OrrificeValve*-model from the TIL-library [47] was used. This valve type allows to change the operating point by regulating the effective flow area of the valve.

3.2.4. Separator

A high-pressure receiver was added to the most basic cycle to extend the part-load operation range, as it helps buffering the varying refrigerant charge in the heat exchangers under different operating conditions [68,69]. The separator imposes saturated conditions at the valve inlet, which will affect the COP as explained in Section 3.1. The ideal separator model of the TIL-library [47] was used, assuming equilibrium conditions at the outlet.

3.2.5. Sensible storage

As this work focuses on the heat pump subsystem, the sensible thermal storage system was not modelled in detail. Instead, a two-tank system with two perfectly homogeneous temperatures was assumed. The water temperature at the inlet of the condenser was thus assumed constant. A boundary model was used to impose a constant inlet temperature and pressure, while the water mass flow rate could be controlled.

3.3. Controller design

The heat pump should respond quickly to a desired power uptake, while maintaining the set storage temperatures and maximizing operational efficiency. Moreover, a low part-load ratio is desirable to maximize the grid balancing capacity that can be offered.

Three parameters were controlled using PI-controllers to obtain this goal: the compressor rotational speed, the valve through-flow area and the water mass flow rate in the condenser.

Variable speed control of the compressor is an effective way to modulate the electrical power uptake [24,27]. Therefore, a first PI-controller compared the desired power uptake (P_{set}) with the effective one (P_{drive}) and changed the rotational speed accordingly. The minimum and maximum saturation value of the compressor speed were set as 25 Hz and 60 Hz, corresponding to the minimum and maximum indicated by the manufacturer [66]. As the operating point is determined by the intersection of the compressor and valve characteristic, a change in compressor speed influences the pressure levels in the cycle. Therefore, a second PI-controller was used to control the effective through-flow area of the valve to maintain a suitable superheat level at the compressor

inlet. A setpoint of 7.5 °C (instead of 3 °C as assumed in the steady-state cycle optimization) was implemented to increase the part-load range and avoid condensation during power ramping. Finally, the water mass flow rate in the condenser was adapted by the third PI-controller to maintain a hot storage temperature of 95 °C by comparing this setpoint to the measured temperature at the condenser outlet. The minimum and maximum saturation values of the controlled valve through-flow area and water mass flow rate in the condenser were chosen as such that the controllers did not reach saturation in any of the simulations.

All PI-constants were determined by analyzing the corresponding system step response of the model without rotational inertia using a dedicated online toolbox [70]. Identical constants were used with inertia as they avoid negative torques (and thus switching to generator mode) during the system step response while maintaining stable system operation and fast response times. The resulting PI-constants and controller saturation values (minimum and maximum) are summarized in Table 8.

3.4. Model validation and verification

All component models used are either based on established models encountered in the literature or are validated against manufacturer data.

The heat exchangers, valve, separator and thermal storage were all modelled using commercially available and validated component models of the TIL-library 3.14.0 [47]. The plate heat exchanger model was used successfully in the literature to simulate the dynamic behavior of large-scale heat pumps [24,50,51]. The sizing related input parameters were based on the literature and the validity ranges of the correlations were verified, as discussed in Section 3.2.1. Similarly, the TIL-models for the valve-, separator- and storage modelling are all based on well-established correlations and were applied in the literature before [24,50,51].

A novel, polynomial-based compressor model was developed for this study as detailed in Section 3.2.2. Empirical models based on performance maps were proven adequate in similar studies analyzing heat pumps using turbomachinery [27,65]. The use of efficiency polynomials to accurately capture this performance data has been demonstrated for volumetric expanders in the literature [71]. In this work, the method was adapted to volumetric compressors. The polynomials were then validated with manufacturer data in Section 3.2.2, demonstrating accurate performance prediction. Another novelty within this work is the inclusion of the compressor rotational inertia within the model. The established equation from traditional mechanics [72] was thus implemented. The rotational inertia of the selected compressor was used, based on the manufacturer data [66].

The full cycle model was thus built up using validated components. The full model could not be validated due to the lack of data on an existing 1.5 MWe heat pump connected to a Carnot battery. Nevertheless, the component sizing, the modelling and the system control were verified by comparison of the steady-state Modelica results to the steady-state Python results of Laterre et al. [35] discussed in Section 3.1. The controllers reached the desired setpoints and realistic parameter values were obtained by the Modelica model. Moreover, the dynamic model behavior was verified by comparison of the obtained response to the little information available in the literature, as will be discussed in Section 4.2.

Table 8
PI-control settings.

Controller	k [−]	T_i [s]	Min sat value	Max sat value
Compressor	0.0000511	3.19	25 Hz	60 Hz
Valve	0.0000463	7.73	0.001 m^2	0.0002 m^2
Water mass flow	1.00	6.99	2 kg/s	60 kg/s

3.5. Regulation time

To quantify and compare the electrical response time, the regulation time, as defined by Meesenburg et al. [24], was used. The regulation time was defined as the time after a step in power uptake setpoint when two criteria are met. First, the absolute deviation of the power uptake P_{drive} should be within a tolerance band of ±1% of full load power uptake P_{nom} (Eq. (2)). Secondly, the gradient of the power uptake should be below $100\,\frac{W}{s}$ (Eq. (3)). The latter is a steady-state condition. Therefore, it may happen that the condition is true but becomes false again before finally reaching the steady state. In this case, the latest time when the condition became true was considered the regulation time.

$$\frac{|P_{drive} - P_{set}|}{P_{nom}} < 0.01\ P_{nom} \tag{2}$$

$$\left|\frac{dP_{drive}}{dt}\right| < 100\frac{W}{s} \tag{3}$$

3.6. Test conditions for ancillary services

The Belgian TSO, Elia, provides prequalification tests for all balancing services discussed in Table 1. All tests follow a similar approach. A power profile representing the most extreme testing situation is provided. The service is then evaluated in terms of full activation time (FAT), maximum power delivery, duration of the service and power deviation. A detailed description of all tests and the corresponding criteria has been added to Appendix A. aFRR and mFRR can deliver either up- or down regulation separately, or do both. The delivery of FCR on the other hand is always symmetric (up and down regulation together) and the offered capacity should react linearly to the frequency deviation of the grid. The minimum bid size for all services is set at 1 MW, but it is allowed to split this capacity over multiple assets. The main criterion is that the requested power uptake or production is (within predefined accuracy) reached within the prescribed FAT. The prequalification tests also aim at verifying if the service can be delivered for a sufficiently long duration. For PTES, this duration is closely related to the capacity and state of charge of the thermal storage system. Here, focus was given to the reaction time and it was assumed the TES was sized adequately, fulfilling the duration requirement.

4. Simulation results and analysis

4.1. Available capacity for balancing services

Heat pumps mostly deliver grid balancing services while they are running already. The service is then delivered by a deviation of the power uptake from the originally scheduled one. This means the range in which the compressor power uptake can be modulated should be determined as it imposes limits on the grid balancing capacity. The minimum part-load power uptake of the system is determined by:

- The minimum rotational speed of the compressor, which is 25 Hz according to the manufacturer data.
- Condensation of the refrigerant at the inlet or outlet of the compressor due to insufficient superheating.
- The condenser temperature, as the heat pump may not be able to sustain a water outlet temperature of 95 °C to the hot storage tank.

The compressor power setpoint was gradually reduced to test which condition limits the part-load capacity of the system. This was done sufficiently slow so that all operating points could be considered steady-state and the operating range was not determined by transient responses. The compressor PI-controller reacts to the decreasing power setpoint by reducing the rotational speed. The PI-controller of the valve and sink consequently react to keep the superheat at the compressor

inlet and the water temperature at the condenser outlet constant. With the implemented control, the minimum rotational speed of the compressor is reached at a power uptake of 750 kW, while the superheat and water outlet temperature remained correct. The minimum part-load capacity of the system is thus determined by the minimum rotational speed of the compressor and the compressor power uptake can be modulated between 750 and 1500 kW. The potential for aFRR and mFRR is hence 750 kW. As FCR should always be delivered symmetrically, the potential power band for FCR is limited to 375 kW around a nominal operating point of 1125 kW.

4.2. Step response: influence of compressor inertia

Before assessing the capability of the system to deliver grid balancing services, it is important to understand the dynamic behavior and system control. Moreover, it is relevant to assess the influence of the compressor inertia modelling. Analyzing this first, gives insight into the prequalification test results later on.

The dynamic behavior is typically studied by analyzing the system's step response. Following the available range of compressor power uptake, a downward and upward step of 750 kW in compressor drive power uptake setpoint (P_{set}) is investigated. The power responses of the model without and with rotational inertia are shown in Fig. 4. The power setpoint is not visible well on the figure as it is covered by the system response with inertia. The variations of the TES-delivery temperature during these power steps are shown in Fig. 5.

From Fig. 4 and Fig. 5 two observations can be made:

- The compressor rotational inertia significantly affects the power response, resulting in lower regulation times when sufficient inertia is present.
- The temperature response is affected by the rotational inertia too. In all cases, the thermal response is delayed compared to the power response. When the compressor inertia is considered, this delay increases but the maximum deviations become smaller.

First, the power response can be analyzed in more detail. The regulation times (see Section 3.4) for the downward and upward step, without and with inertia, are summarized in Table 9. When compressor inertia is neglected, regulation times of 51 s and 55 s were found for the downward and upward step respectively. These values are similar to the response time of 54 s obtained by Meesenburg et al. [24], who made similar modelling and control assumptions. A direct comparison of these results is difficult due to the two-stage lay-out of the heat pump and smaller capacity (250 kWe) of the heat pump modelled by Meesenburg et al. [24]. However, the similar quantitative response times and qualitative system response to a step in power setpoint provide confidence in the current modelling approach. Yang et al. [19] studied the dynamic response of a 5 MWe Brayton-based heat pump integrated in a Carnot battery and applied a 350 kWe ramp over 20 s. The regulation time is not quantified. The 20 s ramping time is thus indicative of the power response, but the criterium on the power deviation is not verified. Despite the different cycle, the order of magnitude is similar to the results found in this work. The modelling results found when neglecting the rotational inertia are thus well aligned with literature.

In Fig. 4, it is visible that the model with inertia follows the power setpoint better than the model without inertia. To understand this counter-intuitive effect of rotational inertia, the power response can be decomposed in its contributing factors: the rotational speed of the compressor axis and the torque at the drive side. These factors are illustrated in Fig. 6. In both cases, speed control is applied to the compressor. When the rotational inertia is neglected, a change in power setpoint is quickly followed by a variation in rotational speed after which it settles quickly on its new steady-state value. However the change in speed is slower when inertia is considered and there is a higher initial torque necessary. Despite the slower speed variation, the desired drive power uptake is thus reached quickly by the corresponding variation in drive torque. The additional rotational resistance of the inertia thus allows to adapt the drive torque based on the power setpoint. It can be said that sufficient rotational inertia effectively decouples the drive side from the refrigerant side, which allows fast power regulation by varying the drive torque.

Finally, an overview of the maximum absolute temperature deviation and thermal response times is given in Table 10. Although the

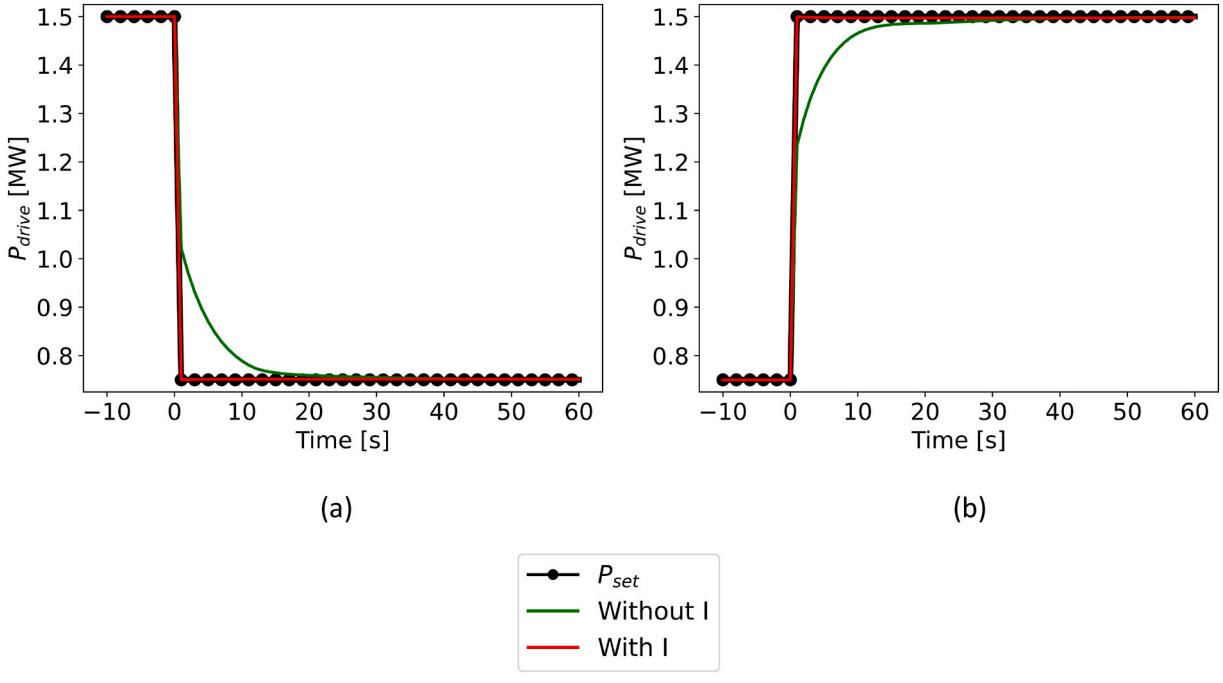

Fig. 4. Power response of a 1.5 MW heat pump to a 750 kW (a) downward and (b) upward step in compressor drive power setpoint.

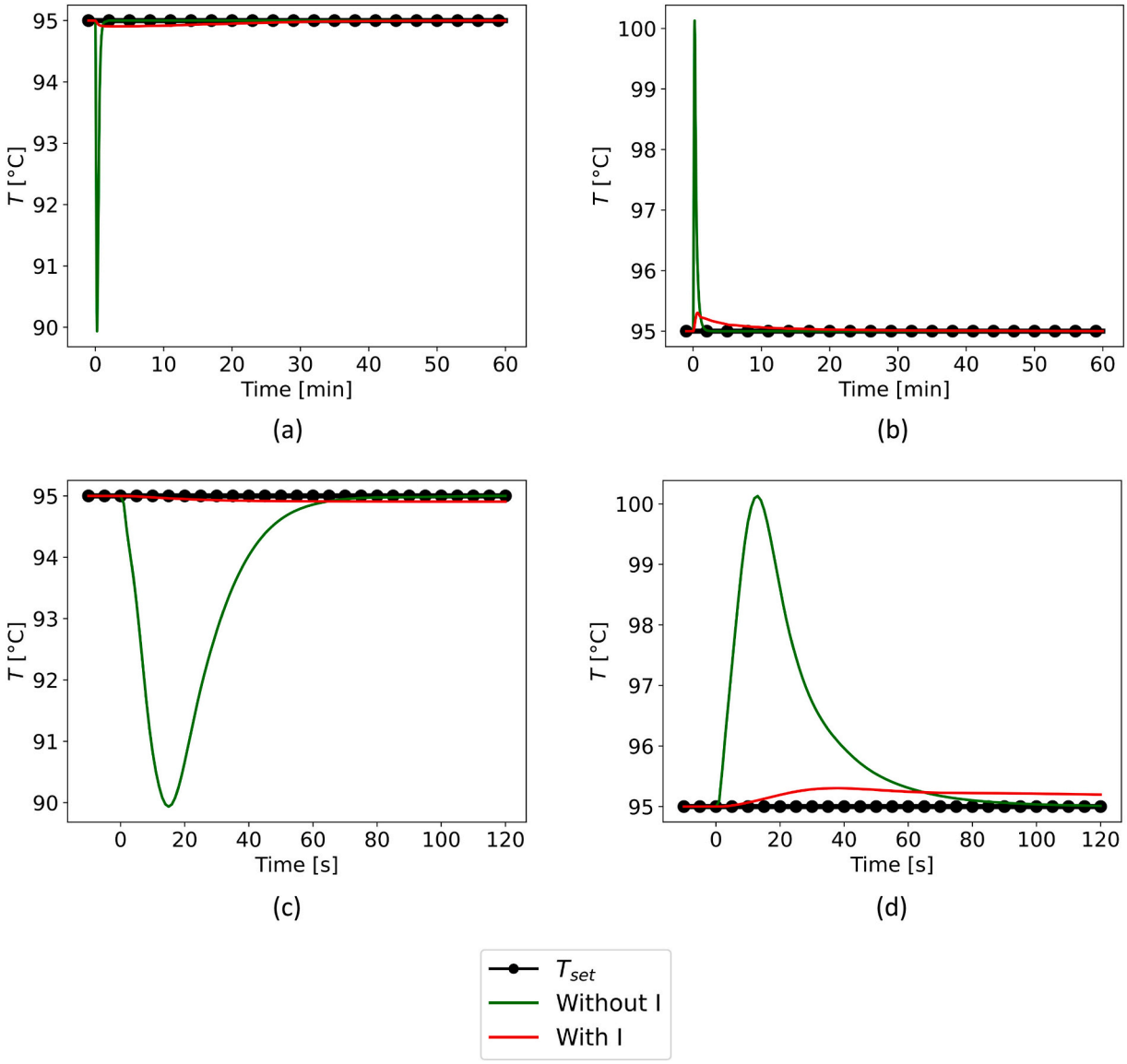

Fig. 5. TES-supply temperature response during a 750 kW (a) downward and (b) upward step in compressor drive power setpoint. Corresponding detailed responses on smaller time scale are shown in (c) and (d) respectively.

Table 9
Regulation time of a 1.5 MWe heat pump to a 750 kW downward and upward step in compressor drive power setpoint.

	$\frac{\lvert P_{drive} - P_{set}\rvert}{P_{nom}} < 0.01\ P_{nom}$	$\left\lvert\frac{dP_{drive}}{dt}\right\rvert < 100\frac{W}{s}$	Regulation time
Downward step – without I	15 s	51 s	51 s
Downward step – with I	0 s	6 s	6 s
Upward step – without I	17 s	55 s	55 s
Upward step – with I	0 s	8 s	8 s

maximum deviation becomes larger than 5 °C when compressor inertia is neglected, it drops below 1 °C within 40 s. When the compressor inertia is considered, the deviations are negligible. The TES-temperature thus remains acceptable during the step response. In all cases, the thermal response is delayed compared to the absolute power variation. When compressor inertia is considered, this delay increases but the maximum deviations become smaller.

This behavior can be understood by analyzing the control sequence in more detail, as visualized in Fig. 7 for a 750 kW upward step in compressor drive power. The response to a downward step is similar. All parameters in Fig. 7 are normalized with the value at the timestep just before the jump in control parameters (t_0) to make the visualization more clear. The control sequence is identical for the model without and with rotational inertia. The PI-controller of the compressor immediately reacts to the increased power setpoint by increasing its rotational speed. The angular acceleration is lower with rotational inertia. As the variation of the cycle parameters is caused by the variation in compressor speed, this explains the delayed and more gradual cycle response with inertia. The increasing compressor speed results in an increased refrigerant mass flow rate ($\dot{m}_r$). Moreover, the condenser pressure increases

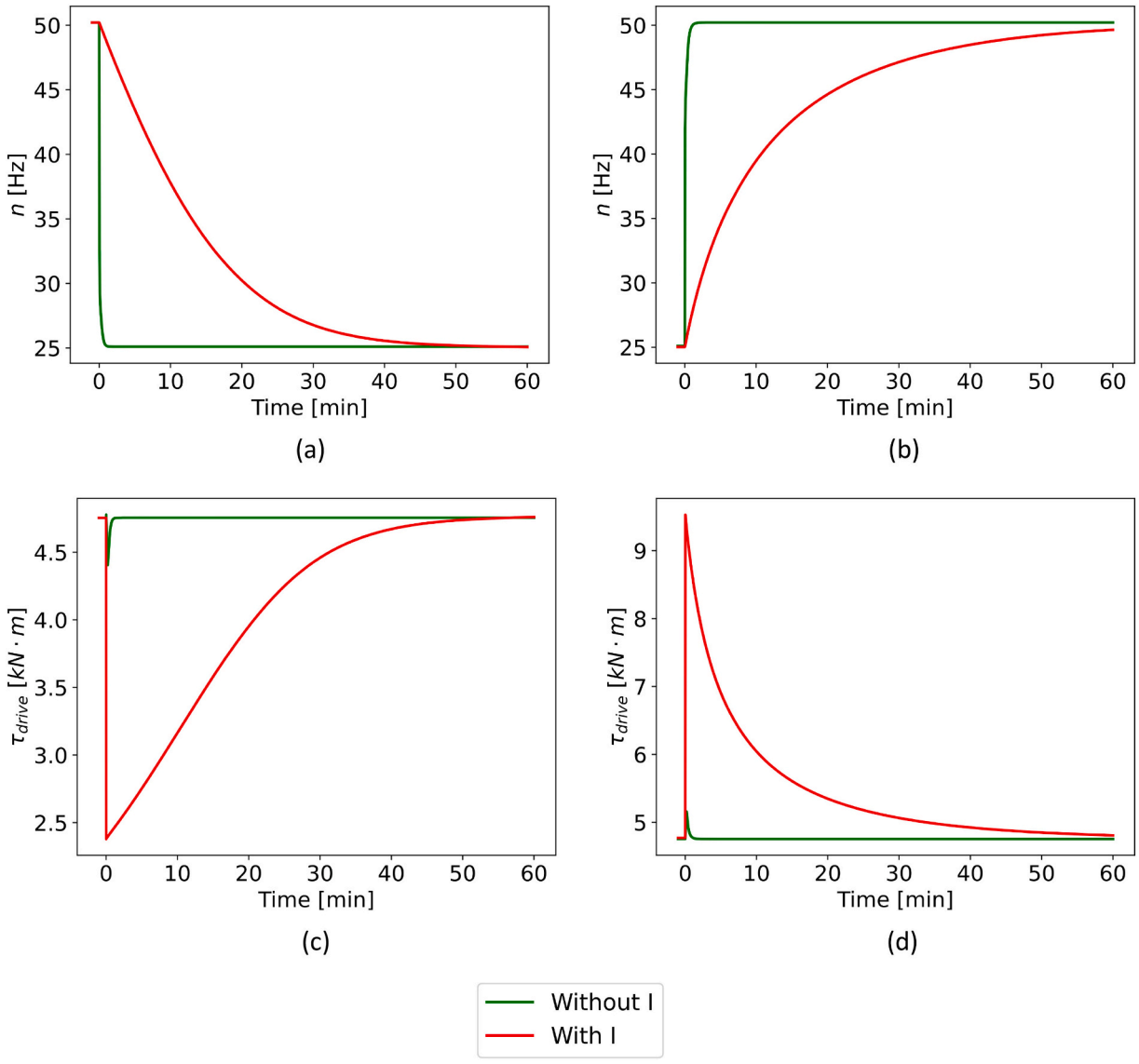

Fig. 6. Variation of the compressor rotational speed and drive torque for a 750 kW (a, c) downward and (b, d) upward step.

Table 10
Maximum absolute temperature deviation and thermal response times of a 1.5 MW heat pump during a 750 kW downward and upward step in compressor drive power setpoint.

Temperature deviation	Max abs deviation [°C]	< 1 °C [s]	< 0.1 °C [s]
Downward step – without I	5.07	40	64
Downward step – with I	0.09	0	0
Upward step – without I	5.13	40	81
Upward step – with I	0.30	0	359

and the evaporator pressure decreases resulting in an increased pressure ratio (PR). The condenser power gradually increases due to the increased refrigerant mass flow rate, but is cushioned by the heat exchanger thermal capacitance. Consequently, the condenser outlet temperature of the water increases. As the heat sink PI-controller reacts on the difference between this outlet temperature and its set value, the controller reaction is thus inherently delayed compared to the compressor PI-controller reacting directly on the desired power uptake at the drive side. Although the power response at the drive side is quicker if rotational inertia is considered, all changes within the refrigerant cycle happen more gradually in this case. Therefore, the sink PI-controller can follow these variations more closely. The refrigerant cycle thus reaches its new steady-state more slowly, but the maximum deviation during the transient remains smaller.

4.3. Prequalification tests for ancillary services

Vapor compression heat pumps for PTES should fulfill two requirements to qualify for prequalification tests: they should pass the service power profile and simultaneously maintain correct charging temperatures to the TES. From the above, it is clear that both these responses are influenced by the rotational inertia of the compressor. Therefore, this inertia is relevant to take this into account during these tests. However, smaller machines may have lower rotational inertia, meaning that the power response depends more on the refrigerant cycle. In practice, this may be encountered when multiple parallel compressors and drives are used. To cover both cases, all prequalification tests were simulated both neglecting and including rotational inertia in the model. As such, the simulation results cover the limiting cases of real systems.

4.3.1. Tertiary reserve

As explained in Appendix A.1. mFRR has a maximum FAT of 12.5 min, which consists of a 2.5 min preparation period and a 10 min

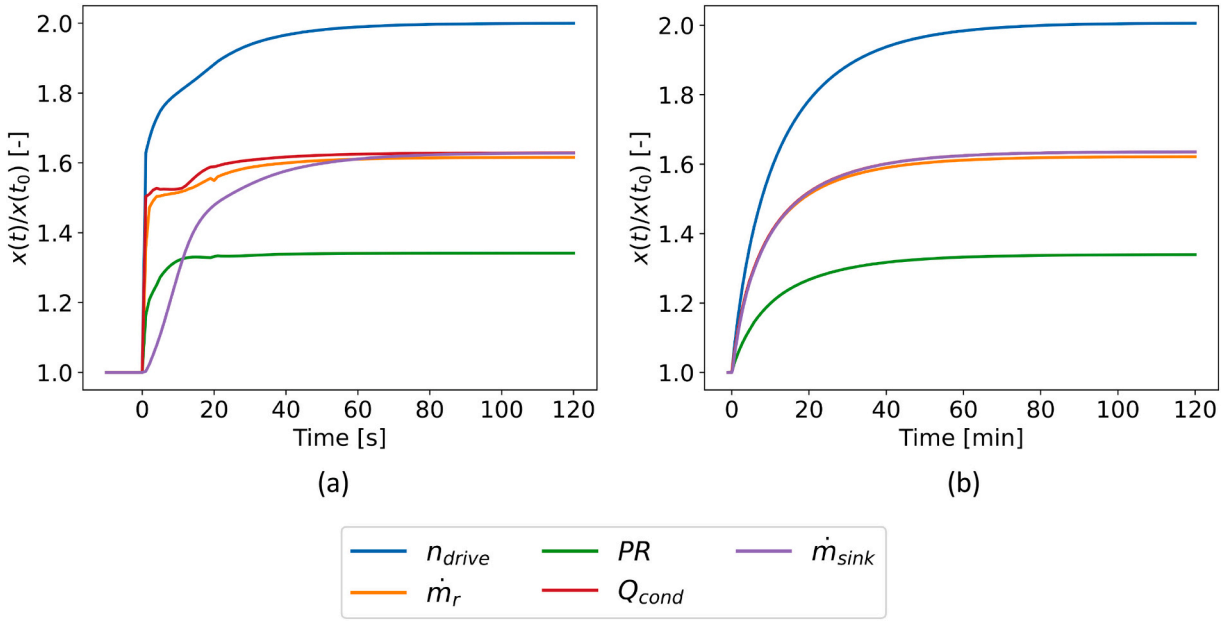

Fig. 7. Visualization of the control sequence for a 750 kW upward step in compressor drive power setpoint (a) without I (b) with I. All values have been normalized with the value at the timestep just before the change is setpoint (t_0).

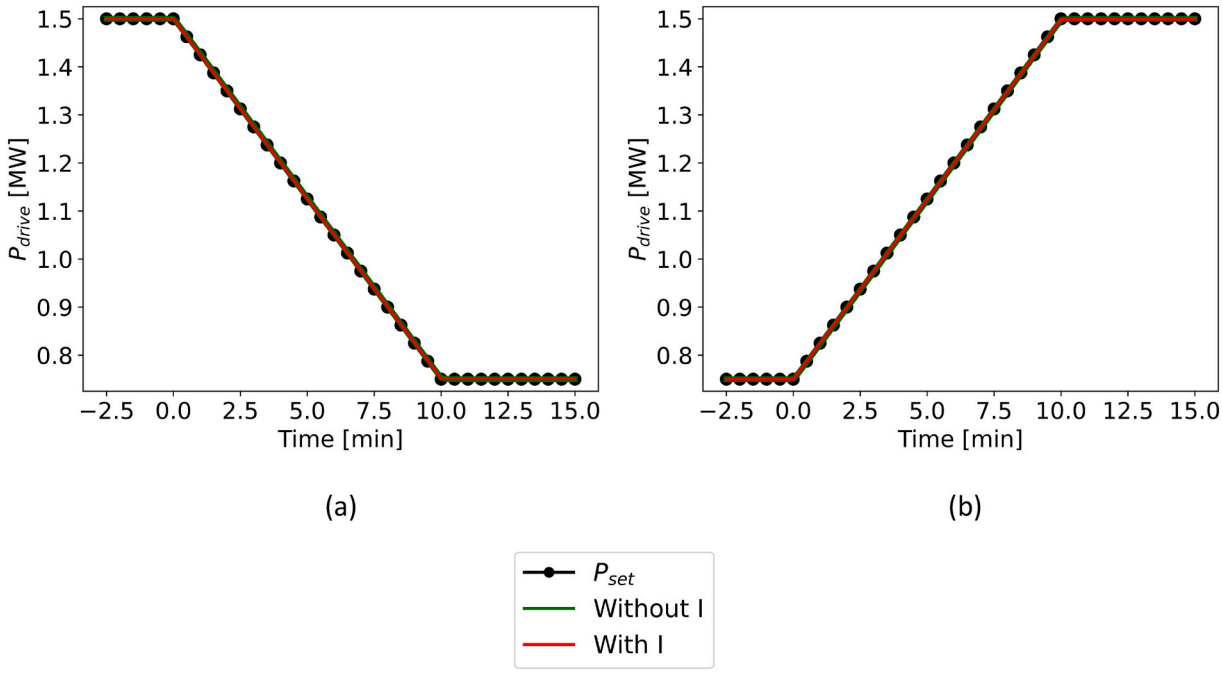

Fig. 8. Power response of a 1.5 MW heat pump to a 750 kW downward (a) and upward (b) ramp in compressor power setpoint.

Table 11
Maximum absolute and relative power deviation between desired and actual power uptake heat pump during mFRR prequalification test.

Maximum power deviation	Absolute (kW)	Relative (%)
mFRR up – without I	2.756	0.33
mFRR up – with I	1.308	0.17
mFRR down – without I	2.774	0.31
mFRR down – with I	1.414	0.10

Table 12
mFRR capacities during prequalification test for mFRR up and mFRR down. Minimum capacities are indicated in bold.

Capacity [kW]	qh4	qh5	qh6	qh7
mFRR up – without I	**749.966**	750	750	750
mFRR up – with I	**748.532**	749.532	749.896	749.976
mFRR down – without I	**749.956**	750	750	750
mFRR down – with I	**749.120**	749.671	749.874	749.940

Table 13
Maximum absolute temperature deviation between desired and actual TES-delivery temperature.

	Maximum temperature deviation [°C]
mFRR up – without I	0.25
mFRR up – with I	0.09
mFRR down – without I	0.25
mFRR down – with I	0.12

ramping period. The power response for mFRR up (reduced power uptake – downward ramp) and mFRR down (increased power uptake – upward ramp) are shown in Fig. 8. The power response without inertia is not clearly visible, as it is partly covered by the response with inertia. The maximum absolute and relative deviations between the setpoint and the actual compressor power uptake at the drive side are summarized in Table 11. A power measurement accuracy of 1 % (with a maximum of 100 kW) over the whole measurement chain is allowed by the TSO. The allowable tolerance thus varies between 7.5 and 15 kW for the studied power range. All observed maximum deviations lie within this allowable tolerance and are thus acceptable. The corresponding supplied mFRR powers for each quarter are summarized in Table 12. As expected, the lowest capacities are found right after activation in all cases. Nevertheless, all values found are within the acceptable tolerance of the desired 750 kW capacity. Therefore, the power response is suitable for a mFRR capacity of 750 kW in both the upward and downward direction.

The corresponding maximum deviations of the water temperature at the condenser outlet are summarized in Table 13. The maximum deviation of 0.25 °C is below the typical accuracy of industrial thermocouples (0.5 to 5 °C) and within the typical accuracy of platinum RTDs (0.1 to 1 °C) [73]. In practice, these deviations are thus acceptable which means the system can deliver mFRR.

4.3.2. Secondary reserve

The aFRR test consists of two main parts: the ramping and full load phase and the follow-up phase (see Appendix A.2. aFRR). Both phases are visible on the power response shown in Fig. 9 for the upward and downward product. It should be noted that the power setpoint and response neglecting rotational inertia are not well visible, as they are covered by the response with inertia.

Table 14
Maximum absolute power deviation between desired and actual power uptake heat pump and number of exceeding allowable tolerance during the load-following phase of the aFRR prequalification test.

	Maximum deviation [kW]	Number of deviations > 7.5 %
aFRR up – without I	3.63	0
aFRR up – with I	1.07	0
aFRR down – without I	3.71	0
aFRR down – with I	1.07	0

Table 15
aFRR capacities during prequalification test for aFRR up and down.

Capacity [kW]	Full power phase	Ramping phase	Prequalified volume
aFRR up – without I	747.653	745.003	745.003
aFRR up – with I	748.643	746.991	746.991
aFRR down – without I	747.324	744.643	744.643
aFRR down – with I	748.374	746.716	746.716

Table 16
Maximum absolute temperature deviation between desired and actual TES-delivery temperature during the aFRR qualification test.

	Maximum temperature deviation [°C]
aFRR up – without I	0.33
aFRR up – with I	0.10
aFRR down – without I	0.33
aFRR down – with I	0.14

The follow-up phase determines successful prequalification and is thus assessed first. During this period, the maximum permitted deviation is 7.5 % of the aFRR power that the balance service provider (BSP) wants to prequalify [14]. For the intended prequalification volume of 750 kW, the allowable margin is thus 56.25 kW. This margin may be exceeded

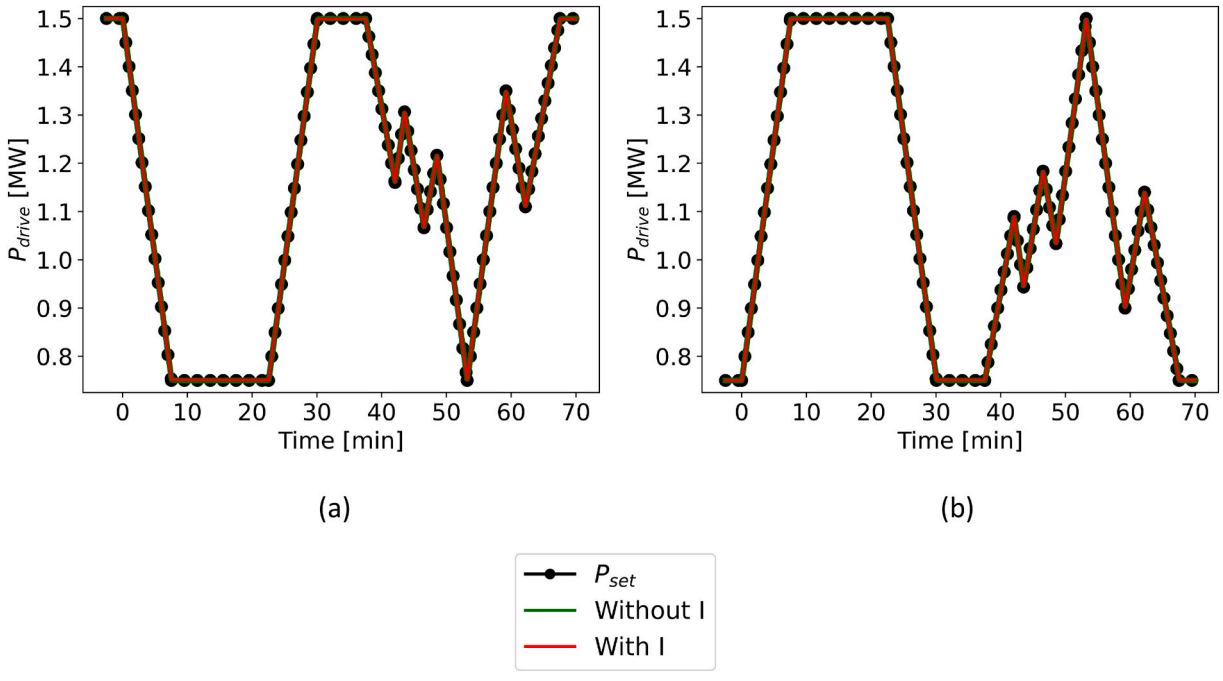

Fig. 9. Power response of a 1.5 MW heat pump to the prequalification test for an upward (a) and downward (b) aFRR capacity.

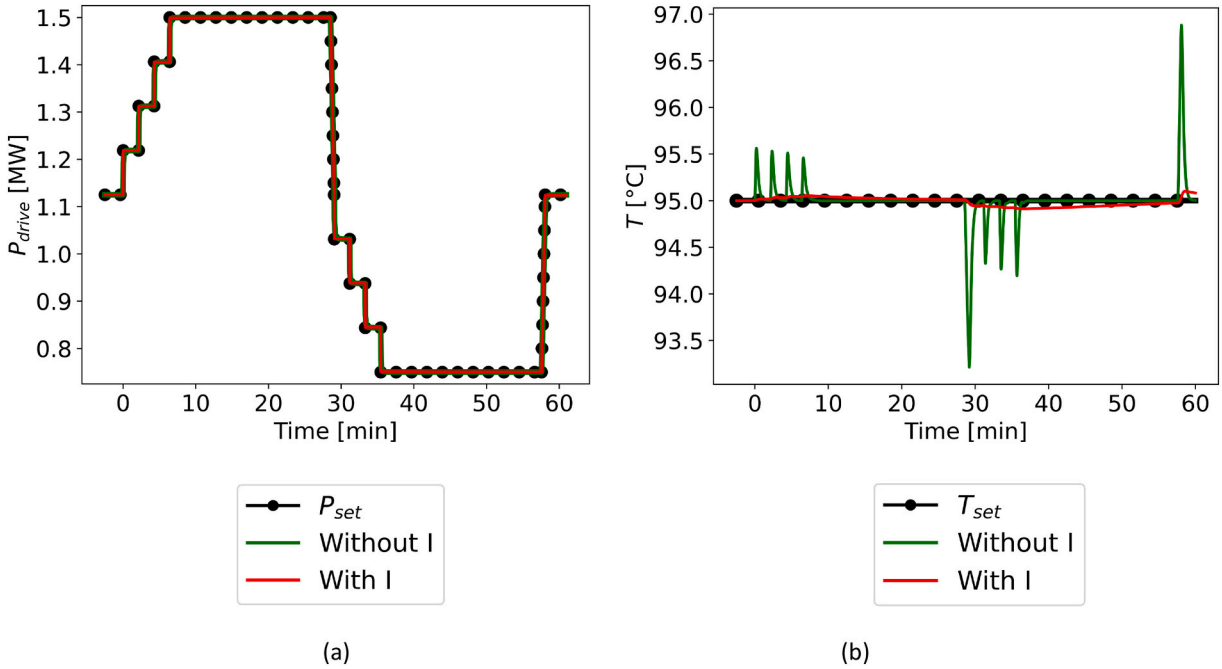

Fig. 10. Power response (a) and water temperature at the condenser outlet (b) during the FCR prequalification test.

Table 17
FCR linearity check test results (according to FCR design note [12]).

Upward steps	1 [kW]	2 [kW]	3 [kW]	4 [kW]
DFCR – without I	90.671	90.401	90.398	90.158
DFCR – with I	93.503	93.506	93.523	93.533
Downward steps	1 [kW]	2 [kW]	3 [kW]	4 [kW]
DFCR – without I	87.654	90.496	91.066	91.180
DFCR – with I	92.920	93.557	93.550	93.540

during 30 timesteps maximally. In Table 14, the maximum power deviation during the load-following tests and number of deviations outside the allowable margin are summarized for the upward and downward product, both without and with inertia in the model. It can be seen all maximum deviations are well below the allowable tolerance, which means the load following test is successfully past in all cases.

Once the load-following test is successfully past, the ramping and full load phase are used to verify the prequalified volume. In Table 15, the volume calculated based on the full power phase and ramping phase are both shown, as well as the final prequalified volume. From this, it can be seen that the ramping phase criterium is determining. Although the prequalified volumes calculated are smaller than the tested volume of 750 kW, this target is within 1 % measurement accuracy from the values obtained.

The maximum absolute temperature deviations of the water temperature at the condenser outlet with respect to the setpoint of 95 °C are summarized in Table 16. The maximum deviations thus remain small. Moreover, the deviation quickly reduces during stable power output periods. Therefore, the temperature response is suitable as well. The system thus qualifies for an aFFR capacity of 750 kW in the upward and downward direction, neglecting and considering rotational inertia.

4.3.3. Primary reserve

The prequalification test for FCR is described in Appendix A.3. FCR. The corresponding compressor power response and TES-supply temperatures are shown in Fig. 10.

To successfully pass the linearity check, at least 90 % of the required FCR capacity has to be activated during each frequency step within 12.5 s [12]. For the symmetric capacity of 375 kW, four steps of 93.75 kW should be taken. Each step should thus at least equal 84.375 kW. As shown in Table 17, this criterium is met for all frequency steps both neglecting and considering rotational inertia. The procedure to determine the corresponding capacity is not detailed in the design note, but included in the Terms & Conditions for balance responsible parties [13]. Following the procedure described, a symmetric FCR capacity of 327 kW and 374 kW are determined for the model without and with inertia. In this document, the magnitude of the frequency step is determined based on 10 s averages which result in a smaller value for the first downward step compared to the minimum value after 12.5 s as described in the design note. This limits the total capacity that can be offered without inertia.

The reaction time constraint prescribes that 50 % of the contracted reserve must be delivered within 15 s and 100 % of the contracted reserve must be delivered within 30 s. Although the synthetic prequalification test includes two 30 s ramps, it is not explicitly described how the reaction time constraint should be evaluated. However, the power set value varies linearly over 30 s and the system response always has a minimal delay which means the total capacity cannot be activated within 30 s. Therefore, it is verified whether the actual power uptake remains within the allowable precision of 1 % during the full load phase and the ramping phases. A summary of the maximum deviations is

Table 18
Maximum relative power deviation during the full load and ramping phase of the FCR prequalification test.

	Upward direction: maximum relative deviation [%]	Downward direction: maximum relative deviation [%]
Without I	2.18	2.32
With I	0.05	0.16

described in Table 18. The required precision is thus not met neglecting rotational inertia, which is caused by the delay of the response during the linear ramping. The system thus not qualifies for FCR when rotational inertia is neglected, while the power response considering this inertia qualifies for a volume of 374 kW, which is within 1 % precision of the 375 kW target.

As visible in Fig. 10 (b), the TES maintains correct storage temperatures. The maximum absolute temperature deviation over the test equals 1.88 and 0.10 °C neglecting and considering rotational inertia respectively and occurs only during the fast ramping from maximal capacity. Therefore, the power response determines the qualification. The system thus qualifies for an FCR capacity of 375 kW when the rotational inertia is considered. This opportunity goes undetected when the rotational inertia is neglected due to the response delay during ramping, which exceeds the allowable deviation for qualification.

Despite this conclusion, it should be noted that the model without rotational inertia has an activation time below 30 s in reaction to a step function in power setpoint as shown in Table 9. Strictly speaking, it thus fulfills the requirement issued by European FCR cooperation [74]. This cooperation prescribes the FAT requirement, but not the prequalification tests to validate it. The Dutch TSO – TenneT – also participates on the same European platform, but prescribes alternative FCR prequalification test profiles [75]. In all but one of these tests, step functions are applied and the power should reach the desired power setpoint within 30 s from the beginning of the step. The one remaining test contains linear ramping. However, in this case the power changes need to be linear and fully achieved within a 30 s delay after ending the ramp. The system neglecting rotational inertia would thus qualify for FCR under the Dutch test conditions, highlighting the need for harmonization of the prequalification tests across all members of the European platform.

5. Conclusion

This work explored the potential to deliver grid balancing services during the charging phase of a Rankine-based PTES. In this context, the electrical power response of the vapor compression heat pump is of interest rather than the thermal response, as it is crucial for integration of the storage system within the electrical grid. A basic 1.5 MWe vapor compression heat pump was modelled dynamically in Modelica to assess this power response. Although the boundary conditions were based on a Carnot battery case study, the model is more generally applicable to large-scale variable-speed heat pumps. After the modelling, a suitable heat pump control strategy driven by the requirements of the electrical grid was implemented. The dynamic system behavior and control with respect to fast electrical power control were analyzed, assessing the influence of compressor rotational inertia modelling on the power response. While this rotational inertia can be considered negligible for thermodynamic performance predictions, which remain dominated by the thermal capacitances and refrigerant reservoirs in the closed loop, the results show it is relevant to variable-speed heat pump applications for correct simulation of the electrical response. Regulation times of 51 and 55 s were found for a 750 kW downward and upward step neglecting compressor inertia, while corresponding times of 6 and 8 s were found when considering this inertia in the model. This illustrates the importance to include the rotational inertia when focusing on the electrical system response. However, smaller machines may have lower rotational inertia, meaning that the electrical response depends more on the characteristics of the refrigeration machine. In practice, this may be encountered when multiple parallel compressors and drives are used. To cover both cases, all prequalification tests were done both neglecting and including rotational inertia in the model. By comparing the power responses of these limiting cases, it was found that systems with sufficient rotational inertia are beneficial for the delivery of grid balancing services. The system can deliver a capacity of 750 kW for aFRR and mFRR in the upward and downward direction, both neglecting and considering rotational inertia. Only when rotational inertia is considered, the system's potential to deliver a symmetric FCR capacity of 375 kW is identified. When rotational inertia is neglected, the system does not pass the prequalification test issued by the Belgian TSO due to a delayed power response during fast ramping. The maximum power deviation of 2.32 % during the ramping phase exceeds the 1 % allowable tolerance. Nevertheless, it still shows fast power dynamics and is hampered by the specific test profile, illustrating the need for harmonization of the prequalification tests between all TSOs on the European platform. Grid balancing services during the charging phase could thus be another revenue stream to increase the financial feasibility of PTES systems and it is thus interesting to explore the potential financial benefits. Given the promising numerical results, it would be worthwhile to experimentally validate them in a real-life demonstrator. In future work, the dynamic model will be extended to a full dynamic Carnot battery model including detailed modelling of the TES and organic Rankine cycle, hence further investigating optimal system scheduling within the energy system.

CRediT authorship contribution statement

Robin Tassenoy: Writing – review & editing, Writing – original draft, Visualization, Validation, Software, Methodology, Investigation, Formal analysis, Conceptualization. **Antoine Laterre:** Writing – review & editing, Methodology, Investigation, Formal analysis. **Vincent Lemort:** Writing – review & editing, Validation, Supervision, Funding acquisition. **Francesco Contino:** Writing – review & editing, Validation, Supervision, Funding acquisition, Conceptualization. **Michel De Paepe:** Writing – review & editing, Validation, Supervision, Resources, Project administration, Methodology, Investigation, Funding acquisition, Formal analysis, Conceptualization. **Steven Lecompte:** Writing – review & editing, Validation, Supervision, Resources, Project administration, Methodology, Investigation, Funding acquisition, Formal analysis, Conceptualization.

Declaration of competing interest

The authors declare that they have no known competing financial interests or personal relationships that could have appeared to influence the work reported in this paper.

Data availability

Data will be made available on request.

Acknowledgements

The authors thank Joannes Laveyne for the interesting discussions on the functioning of the electrical energy system and grid balancing services. They also thank Yves Maenhout for his technical support, looking after the calculation server and software used. The second author acknowledges the support of Fonds de la Recherche Scientifique - FNRS [40014566 FRIA-B1].

Appendix A

This appendix provides a more detailed description of the different grid balancing services and their criteria, as issued Elia, the Belgian TSO.

A.1. mFRR

A European platform for the exchange of balancing energy from frequency restoration reserves with manual activation is currently developed within the Manually Activated Reserves Initiative (MARI) [76]. Currently, Elia is a non-operational MARI member, meaning it participated in the definition of the uniform services, but is currently not yet connected to the European platform. Recently, the required changes in design to the Belgian mFRR service to connect to the central European mFRR platform were published [16]. Therefore, the updated prequalification test is used in this study already although it is not yet effective. A visual representation of this test is given in Fig. 11.

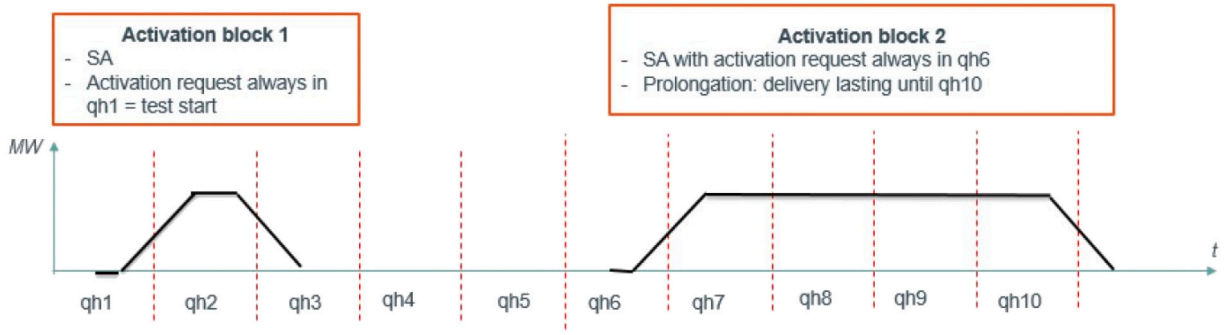

Fig. 11. Prequalification test for mFRR within the MARI project (as in [16]).

This prequalification test was updated to take into account the European activation types and profiles. The full test lasts 10 quarter-hours and consists of two activation blocs with a non-activation pause in between. The first activation block consists of one quarter-hour scheduled activation. The second block consists of a scheduled activation in the sixth quarter-hour and should last until qh10. After sending the signal for activation, a 2.5 min preparation period is respected after which the power is ramped to full capacity over a period of 10 min. Therefore, the full activation time is 12.5 min.

Elia determines the energy, and from this the power, that is supplied for each quarter hour of delivery in the test (qh2, qh7, qh8, qh9, qh10). When testing one delivery point, the prequalified volume equals the minimum power supplied during one of these quarter-hours and is the maximum offer for a mFRR capacity auction.

As this work focuses on the power response and the energy requirement is assumed fulfilled, the test has been simplified as an upward and downward ramp over 10 min respectively. The power was then kept at the desired mFRR capacity for 4 quarter hours to determine the minimum capacity delivered.

A.2. aFRR

Similar to the MARI platform, the Platform for the International Coordination of Automated Frequency Restoration and Stable System Operation (PICASSO) aims to exchange balancing energy from aFRR between the European TSOs [77]. At the moment of writing, Elia is an non-operational member of the PICASSO project and is thus not yet connected to this platform [15]. The design note discussing the required changes to the current Belgian aFRR service was not published at the moment of writing. Therefore, the effective prequalification test as described in the dedicated design note [14], was used. A visual representation of the test is given in Fig. 12.

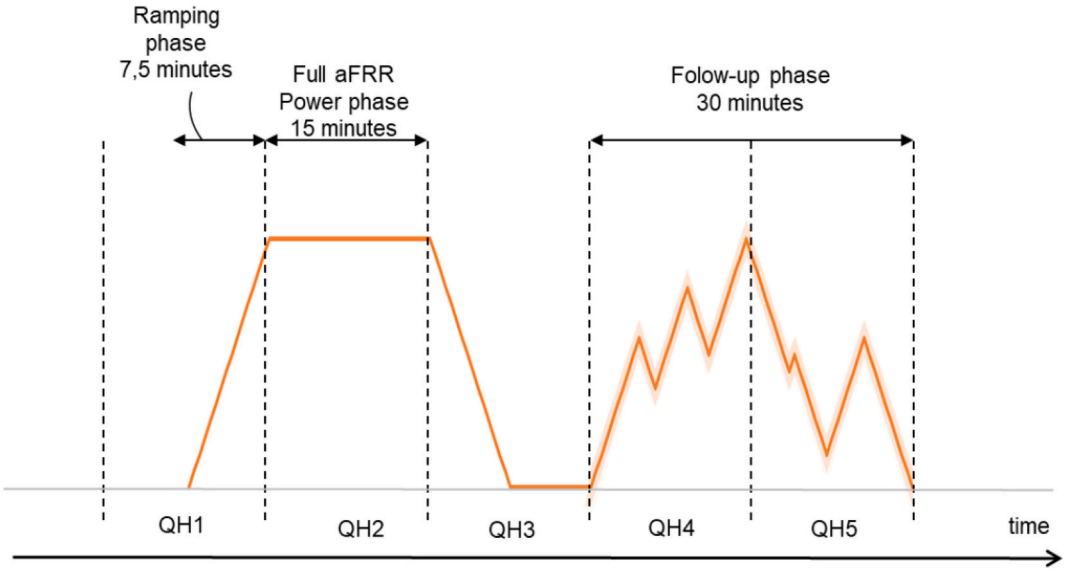

Fig. 12. Prequalification test for aFRR (as in [14]).

The test consists of two main parts: the ramping and full load phase and the follow-up phase. The follow-up phase tests the load-following capacity of the system and determines successful prequalification. The first part is similar to the mFRR test and is used to determine the corresponding maximum capacity the system can offer.

The prequalification test is successful if the deviation between the requested and delivered aFRR power remains within a margin of 7.5 % during the follow-up phase. A maximum of 30 deviations larger than this margin is allowed [14].

For each successful prequalification test, the maximum capacity is determined from the first part of the test. In the ramping phase, the system has to ramp to full aFRR capacity in 7.5 min. Then, it should sustain this capacity for 15 min in the full power phase. The offered capacity is then calculated as the minimum of:

(1) The minimum aFRR power supplied during the full power phase, excluding the two lowest values.
(2) The difference between the maximum aFRR power supplied and the minimum aFRR power supplied during the last 7.5 min of the ramping phase.
(3) The minimum aFRR power the balance responsible party wishes to prequalify.

A.3. FCR

Finally, FCR is considered. As illustrated in Table 1 this service requires the fastest response time and a bid should be offered symmetrically. The Belgian TSO, Elia, participates in the European FCR cooperation, along with 11 other TSOs from 8 other countries [74]. Its prequalification tests are thus aligned with the requirements of this European platform. Two tests are issued: the synthetic frequency profile and the follow up of real time frequency [12]. These tests are visualized in Fig. 13.

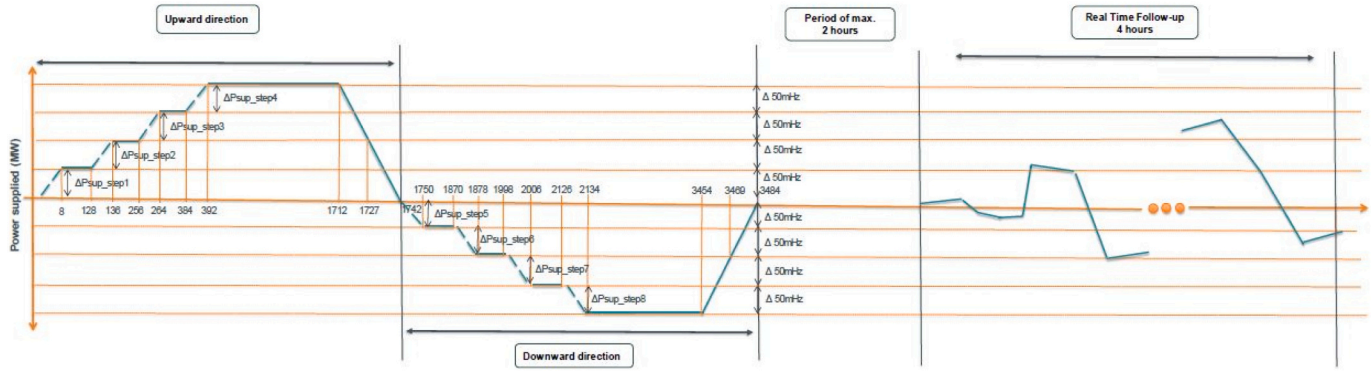

Fig. 13. FCR prequalification test (as in [13]).

The synthetic frequency profile aims at verifying the linearity of the FCR reaction, the continuous activation at full capacity for a set duration and the reaction time constraint [12]. The synthetic load profile makes up the first phase of the test. It is composed of a combined test in the upward and downward direction. Each direction is composed of four parts [13]:

- First, four frequency steps of 50 mHz are imposed. The corresponding FCR power should be reached within 12.5 s (7.5 s of required activation time and 5 s of tolerance). This FCR power should then be maintained for 2 min.
- The full capacity is tested by maintaining the full FCR power for 22 min after the fourth frequency step.
- After this period of 22 min, the FCR power is ramped down to zero in 30 s to test the system response time. According to the design note [12], 50 % of the contracted reserve (to be delivered when the frequency deviation reaches 100 mHz) should be delivered within 15 s. 100 % of the contracted reserve must be delivered within 30 s.

Successful participation in the load following test is evaluated as follows [12]:

- The minimal power value at each frequency step of 50 mHz (over a period of 120 s) will be taken as reference value for the related step.
- At least 90 % (tolerance margin of 10 % allowed) of the required FCR capacity must be activated at each step to consider the linearity check valid.
- 5 s margin is allowed in addition to the required activation time (7.5 s) before Elia considers the tele-measurements to determine the minimal value of the step. The minimal values are thus measured starting from 12.5 s after imposing the step.
- The lowest result for a specific step (of both upward and downward tests) determines the total prequalified FCR volume.

This procedure to determine the qualified capacity is described numerically in the terms & conditions for balance responsible parties [13].

While the synthetic load profile test aims at verifying the technical capacity of the system to deliver FCR, the real time follow up test aims to verify the continuous activation reacting on the actual frequency variation of the grid. This test part was disregarded in this study as it focusses on the technical system requirements.

References

[1] Enerdata, World Energy & Climate Statistics - Yearbook 2023 - Renewable in electricity production share [cited 2023 25/09/2023]; Available from: https://yearbook.enerdata.net/renewables/renewable-in-electricity-production-share.html, 2023.
[2] M.C. Argyrou, P. Christodoulides, S.A. Kalogirou, Energy storage for electricity generation and related processes: technologies appraisal and grid scale applications, Renew. Sustain. Energy Rev. 94 (2018) 804–821.
[3] European Commission, et al., Study on energy storage: contribution to the security of the electricity supply in Europe, Publications Office Editor, 2020.
[4] O. Schmidt, I. Staffell, Monetizing Energy Storage: A Toolkit to Assess Future Cost and Value, Oxford University Press, 2023.
[5] J.D. McTigue, et al., Techno-economic analysis of recuperated joule-Brayton pumped thermal energy storage, Energ. Conver. Manage. 252 (2022).
[6] O. Dumont, et al., Carnot battery technology: a state-of-the-art review, Journal of Energy Storage (2020) 32.
[7] A. Vecchi, et al., Carnot battery development: a review on system performance, applications and commercial state-of-the-art, Journal of Energy Storage (2022) 55.
[8] F. Braeuer, et al., Battery storage systems: an economic model-based analysis of parallel revenue streams and general implications for industry, Appl. Energy 239 (2019) 1424–1440.
[9] S. Yamujala, et al., Multi-service based economic valuation of grid-connected battery energy storage systems, Journal of Energy Storage (2022) 52.
[10] J. Villar, R. Bessa, M. Matos, Flexibility products and markets: literature review, Electr. Pow. Syst. Res. 154 (2018) 329–340.
[11] J. Hjalmarsson, K. Thomas, C. Boström, Service stacking using energy storage systems for grid applications – a review, Journal of Energy Storage (2023) 60.
[12] Elia, FCR service design note: Market Development, 2019, p. 50.
[13] Elia, Terms and Conditions for Balancing Service Providers of Frequency Containment Reserve (FCR) ("T&C BSP FCR"), 2020.
[14] Elia, in: Elia (Ed.), Terms and Conditions for balancing service providers for automatic Frequency Restoration Reserve (aFRR) ("T&C BSP aFRR"), 2023, p. 106.
[15] Elia, Keeping the Balance: Automatic Frequency Restoration Process (aFRR/R2) [cited 2024 15/01/2024]; Available from: https://www.elia.be/en/electricity-market-and-system/system-services/keeping-the-balance/afrr, 2024.
[16] Elia, Design note - Balancing services: mFRR - The design for manual Frequency Restoration Reserves (mFRR) in the Elia LFC Block in the framework of the European platform for mFRR energy exchanges (MARI), 2022, p. 83.
[17] C. Lu, et al., Dynamic modeling and numerical investigation of novel pumped thermal electricity storage system during startup process, Journal of Energy Storage (2022) 55.
[18] A. Laterre, et al., Is waste heat recovery a promising avenue for the Carnot battery? Techno-economic optimisation of an electric booster-assisted Carnot battery integrated into different data centres, Energ. Conver. Manage. 301 (2024).
[19] H. Yang, et al., Dynamic characteristics and control strategy of pumped thermal electricity storage with reversible Brayton cycle, Renew. Energy 198 (2022) 1341–1353.
[20] X.J. Xue, C.Y. Zhao, Transient behavior and thermodynamic analysis of Brayton-like pumped-thermal electricity storage based on packed-bed latent heat/cold stores, Appl. Energy 329 (2023).
[21] V. Sánchez-Canales, et al., Dynamic modelling and techno-economic assessment of a compressed heat energy storage system: application in a 26-MW wind farm in Spain, Energies 13 (18) (2020).
[22] D. Canpolat Tosun, et al., Dynamic performance and sustainability assessment of a PV driven Carnot battery, Energy 278 (2023).
[23] A. Tafone, et al., Dynamic modelling of a compressed heat energy storage (CHEST) system integrated with a cascaded phase change materials thermal energy storage, Appl. Therm. Eng. 226 (2023).
[24] W. Meesenburg, et al., Optimizing control of two-stage ammonia heat pump for fast regulation of power uptake, Appl. Energy 271 (2020).
[25] L. Wolscht, et al., Dynamic simulation and experimental validation of a 35 MW heat pump based on a transcritical CO2 cycle, Energy 294 (2024).
[26] A. David, et al., Heat roadmap Europe: large-scale electric Heat pumps in district heating systems, Energies 10 (4) (2017).
[27] L. Wolscht, et al., Dynamic Simulation and Experimental Validation of a 35 MW Heat Pump Based on a Transcritical CO2 Cycle, in the 5th European sCO2 Conference for Energy Systems, Czech Republic, Prague, 2023.
[28] M. Imran, et al., Dynamic modeling and control strategies of organic Rankine cycle systems: methods and challenges, Appl. Energy 276 (2020).
[29] R. Pili, et al., Simulation of organic rankine cycle – quasi-steady state vs dynamic approach for optimal economic performance, Energy 167 (2019) 619–640.
[30] G.F. Frate, M. Antonelli, U. Desideri, A novel pumped thermal electricity storage (PTES) system with thermal integration, Appl. Therm. Eng. 121 (2017) 1051–1058.
[31] A. Marina, et al., An estimation of the European industrial heat pump market potential, Renew. Sustain. Energy Rev. 139 (2021).
[32] G.F. Frate, L. Ferrari, U. Desideri, Multi-criteria economic analysis of a pumped thermal electricity storage (PTES) with thermal integration, Frontiers in Energy Research (2020) 8.
[33] A. Rahman, A.D. Smith, N. Fumo, Performance modeling and parametric study of a stratified water thermal storage tank, Appl. Therm. Eng. 100 (2016) 668–679.
[34] A. Dahash, et al., Advances in seasonal thermal energy storage for solar district heating applications: a critical review on large-scale hot-water tank and pit thermal energy storage systems, Appl. Energy 239 (2019) 296–315.
[35] A. Laterre, et al., Extended mapping and systematic optimisation of the Carnot battery trilemma for sub-critical cycles with thermal integration, Energy 304 (2024).
[36] C. Arpagaus, et al., High temperature heat pumps: market overview, state of the art, research status, refrigerants, and application potentials, Energy 152 (2018) 985–1010.
[37] B. Zühlsdorf, et al., Annex 58 High-Temperature Heat Pumps Task 1 - Technologies, 2023.
[38] M. Lindahl, et al., in: I.H.P. Technologies (Ed.), IEA Heat Pumping Technologies Annex 57: flexibility by implementation of heat pumps in multi-vector energy systems and thermal networks - Task 4 report: Flexibility Assessment and Analyses of different options, IEA Heat Pumping Technologies Annex 57, 2023, p. 37.
[39] G.F. Frate, L. Ferrari, U. Desideri, Analysis of suitability ranges of high temperature heat pump working fluids, Appl. Therm. Eng. 150 (2019) 628–640.
[40] B. Eppinger, et al., Pumped thermal energy storage with heat pump-ORC-systems: comparison of latent and sensible thermal storages for various fluids, Appl. Energy 280 (2020).
[41] E.W. Lemmon, et al., NIST Standard Reference Database 23: Reference Fluid Thermodynamic and Transport Properties - REFPROP, Version 10.0, National Institute of Standards and Technology, 2018.
[42] J.J. Brasz, Comparison of Part-Load Efficiency Characteristics of Screw and Centrifugal Compressors, in: International Compressor Engineering Conference, 2006, p. 7. West Lafayette, IN, USA.
[43] E. Vieren, et al., The thermodynamic potential of high-temperature transcritical heat pump cycles for industrial processes with large temperature glides, Appl. Therm. Eng. 234 (2023).
[44] B. Zühlsdorf, et al., Analysis of technologies and potentials for heat pump-based process heat supply above 150 °C, Energ. Conver. Manage. X (2019) 2.
[45] Modelica Association, Modelica and the Modelica Standard Library, 2023.
[46] Dassault systemes, Dymola 2022, 2022.
[47] T.L.K. Energy, TIL Suite - the Library for Thermodynamic Systems, 2023.
[48] Funke, Plate Heat Exchangers: series FP, FPDW, 2023.
[49] Plate Heat Exchangers - Design, Applications and Performance, in: L. Wang, B. Sundén, R.M. Manglik (Eds.), International Series on Developments in Heat Transfer, ed. B. Sundén, WIT Press, Southampton, UK, 2007.
[50] W. Meesenburg, et al., Operation of large-scale heat pumps under fluctuating boundary conditions, in: 26th International Congress of Refrigeration, 2023. Paris, France.
[51] K.R. Kramer, et al., Analysis of Large- Scale Ammonia Heat Pumps in Transient Operating Conditions, in: 14th IEA Heat Pump Conference 2023, 2023. Chicago, USA.
[52] T. Kuppan, Heat exchanger design handbook, Marcel Dekker, Inc, New York, USA, 2000.
[53] D. Lee, et al., Evaporation heat transfer coefficient and pressure drop of R-1233zd (E) in a brazed plate heat exchanger, Appl. Therm. Eng. 130 (2018) 1147–1155.
[54] J. Zhang, et al., Condensation heat transfer and pressure drop characteristics of R134a, R1234ze(E), R245fa and R1233zd(E) in a plate heat exchanger, International Journal of Heat and Mass Transfer 128 (2019) 136–149.
[55] J. Zhang, B. Elmegaard, F. Haglind, Condensation heat transfer and pressure drop correlations in plate heat exchangers for heat pump and organic Rankine cycle systems, Appl. Therm. Eng. 183 (2021).
[56] J.R. García-Cascales, et al., Assessment of boiling and condensation heat transfer correlations in the modelling of plate heat exchangers, Int. J. Refrig. 30 (6) (2007) 1029–1041.
[57] H. Martin, N6 pressure drop and heat transfer in plate heat exchangers, in: VDI Heat Atlas, Springer, Berlin, Heidelberg, 2010, pp. 1515–1522.
[58] G.A. Longo, et al., A new model for refrigerant boiling inside Brazed Plate Heat Exchangers (BPHEs), International Journal of Heat and Mass Transfer 91 (2015) 144–149.
[59] G.A. Longo, G. Righetti, C. Zilio, A new computational procedure for refrigerant condensation inside herringbone-type Brazed Plate Heat Exchangers, Int. J. Heat Mass Transf. 82 (2015) 530–536.
[60] K. Hoopes, T.C. Allison, R. Kurz, Oil and Gas Compressor Basics, in Compression Machinery for Oil and Gas, 2019, pp. 3–11.
[61] V. Lemort, Contribution to the Characterization of Scroll Machines in Compressor and Expander Modes, in Faculty of the University of Liège, University of Liège: Liège, Belgium, 2008.
[62] A. Giuffrida, A semi-empirical method for assessing the performance of an open-drive screw refrigeration compressor, Appl. Therm. Eng. 93 (2016) 813–823.
[63] F. Kaufmann, et al., Development of a generalised low-order model for twin-screw compressors, in: 7th international Seminar on O.R.C. Power Systems, 2023, p. 10. Seville, Spain.
[64] O. Dumont, R. Dickes, V. Lemort, Extrapolability and limitations of a semi-empirical model for the simulation of volumetric expander, in: IV International Seminar on ORC Power Systems, ORC2017 8, 2017. Milano, Italy.
[65] R. Tassenoy, et al., Numerical performance assessment of heat pumps in Rankine-based Carnot battery systems for grid balancing services, in: 14th IEA Heat Pump Conference, 2023, p. 12. Chicago, IL, USA.
[66] GEA Heating & Refrigeration Technologies, RTSelect Software - GEA Heating & Refrigeration Technologies, 2024.
[67] G. Van Rossum, F.I. Drake, CreateSpace (Eds.), Python 3 Reference Manual, 2009. Scotts Valley, CA, USA.
[68] V. Pomme, Improved Automotive A/C Systems Using a New Forced Subcooling Technique, in SAE International Congress and Exposition, Society of Automotive Engineers, Inc., Detroit, Michigan, USA, 1999.

[69] Steady state and dynamic modelling of a 1 MWel commercial waste heat recovery ORC power plant, in: G. Andritos, , et al.A. Kitanovski, A. Poredos (Eds.), 29th International Conference on Efficiency, Cost, Optimisation, Simulation and Environmental Impact of Energy Systems, Faculty of Mechanical Engineering, Ljubljana, Portoroz, Slovenia, 2016.
[70] PidTuner, PID Tuner Controller - Tune your PID, 2023.
[71] K. Couvreur, et al., Experimental and numerical analysis of variable volume ratio as additional optimization parameter in organic Rankine cycle expanders, Appl. Therm. Eng. 216 (2022).
[72] H.D. Young, R.A. Freedman, A.L. Ford, in: J. Zalensky (Ed.), University Physics with Modern Physics, 14th edition, global edition. 14th edition ed, Pearson Education Limited, Essex, England, 2016, p. 1593.
[73] RS Pro, RS Pro - Platinum Resistance Thermometer (PRT) Selection Guide, 2024.
[74] ENTSO-E, Frequency Containment Reserves [cited 2024 15/01/2024]; Available from: https://www.entsoe.eu/network_codes/eb/fcr/, 2024.
[75] TenneT, FCR Manual for BSP's: Requirements and procedures for supply of FCR, 2022, p. 33.
[76] ENTSO-E, Manually Activated Reserves Initiative (MARI) [cited 2024 08/01/2024]; Available from: https://www.entsoe.eu/network_codes/eb/mari/, 2024.
[77] ENTSO-E, PICASSO [cited 2024 15/01/2024]; Available from: https://www.entsoe.eu/network_codes/eb/picasso/, 2024.